




# The Spike-Stabilizing D614G Mutation Interacts with S1/S2 Cleavage Site Mutations To Promote the Infectious Potential of SARS-CoV-2 Variants

Stacy Gellenoncourt,<sup>a</sup> Nell Saunders,<sup>a</sup> Rémy Robinot,<sup>a</sup> Lucas Auguste,<sup>a,b</sup> Maaran Michael Rajah,<sup>a</sup> Jérôme Kervevan,<sup>a</sup> Raphaël Jeger-Madiot,<sup>a</sup> Isabelle Staropoli,<sup>a</sup> Cyril Planchais,<sup>c</sup> Hugo Mouquet,<sup>c</sup> Julian Buchrieser,<sup>a</sup> Olivier Schwartz,<sup>a,d</sup>  Lisa A. Chakrabarti<sup>a</sup>

<sup>a</sup>Virus & Immunity Unit, Institut Pasteur, Université Paris Cité, CNRS UMR 3569, Paris, France

<sup>b</sup>Université de Nîmes, Nîmes, France

<sup>c</sup>Laboratory of Humoral Immunology, Institut Pasteur, Université Paris Cité, Paris, France

<sup>d</sup>Vaccine Research Institute, Créteil, France

**ABSTRACT** Severe acute respiratory syndrome coronavirus 2 (SARS-CoV-2) remained genetically stable during the first 3 months of the pandemic, before acquiring a D614G spike mutation that rapidly spread worldwide and then generating successive waves of viral variants with increasingly high transmissibility. We set out to evaluate possible epistatic interactions between the early-occurring D614G mutation and the more recently emerged cleavage site mutations present in spike of the Alpha, Delta, and Omicron variants of concern. The P681H/R mutations at the S1/S2 cleavage site increased spike processing and fusogenicity but limited its incorporation into pseudoviruses. In addition, the higher cleavage rate led to higher shedding of the spike S1 subunit, resulting in a lower infectivity of the P681H/R-carrying pseudoviruses compared to those expressing the Wuhan wild-type spike. The D614G mutation increased spike expression at the cell surface and limited S1 shedding from pseudovirions. As a consequence, the D614G mutation preferentially increased the infectivity of P681H/R-carrying pseudoviruses. This enhancement was more marked in cells where the endosomal route predominated, suggesting that more stable spikes could better withstand the endosomal environment. Taken together, these findings suggest that the D614G mutation stabilized S1/S2 association and enabled the selection of mutations that increased S1/S2 cleavage, leading to the emergence of SARS-CoV-2 variants expressing highly fusogenic spikes.

**IMPORTANCE** The first SARS-CoV-2 variant that spread worldwide in early 2020 carried a D614G mutation in the viral spike, making this protein more stable in its cleaved form at the surface of virions. The Alpha and Delta variants, which spread in late 2020 and early 2021, respectively, proved increasingly transmissible and pathogenic compared to the original strain. Interestingly, Alpha and Delta both carried the mutations P681H/R in a cleavage site that made the spike more cleaved and more efficient at mediating viral fusion. We show here that variants with increased spike cleavage due to P681H/R were even more dependent on the stabilizing effect of the D614G mutation, which limited the shedding of cleaved S1 subunits from viral particles. These findings suggest that the worldwide spread of the D614G mutation was a prerequisite for the emergence of more pathogenic SARS-CoV-2 variants with highly fusogenic spikes.

**KEYWORDS** SARS-CoV-2, epistasis, proteolytic cleavage, spike, variants

The severe acute respiratory syndrome coronavirus 2 (SARS-CoV-2) pandemic has remained a major public health issue during the past 2 years, due to the repeated emergence of viral variants endowed with increased transmissibility and/or immune

**Editor** Tom Gallagher, Loyola University Chicago

**Copyright** © 2022 American Society for Microbiology. All Rights Reserved.

Address correspondence to Lisa A. Chakrabarti, [chakra@pasteur.fr](mailto:chakra@pasteur.fr).

The authors declare no conflict of interest.

**Received** 19 August 2022

**Accepted** 30 August 2022

**Published** 19 September 2022

escape capacity, leading to successive epidemic rebounds (1). The SARS-CoV-2 virus is a beta-coronavirus characterized by a relatively low mutation rate (2), but the sheer length of its RNA genome (30 kb) and its wide dissemination provide ample opportunities for the emergence and selection of viral mutations. SARS-CoV-2 remained genetically stable during the first few months of the pandemic, before the emergence in February-March 2020 of a variant characterized by a D614G mutation in the spike gene (3). The spread of the D614G mutation proved remarkably rapid, as this mutation achieved worldwide dominance by June 2020 and has remained present in the vast majority of SARS-CoV-2 genomes sequenced so far (4). The end of 2020 was marked by the independent emergence of divergent SARS-CoV-2 lineages: B.1.1.7 in the United Kingdom, B.1.351 in South Africa, and P1 in Brazil. These new lineages were associated with rapid epidemic rebounds and have since been renamed the Alpha, Beta, and Gamma variants of concern (VOC), respectively (5). The emergence of the VOC could be ascribed to an increase in transmissibility and in escape from innate immunity in the case of the Alpha variant (6–8) and to an efficient escape from preexisting neutralizing antibody responses in the case of the Beta and Gamma variants (9, 10). Other emerging lineages characterized by a more localized spread, such as Kappa and Epsilon, were labeled as variants of interest (VOI). February 2021 saw the emergence of the B.1.617 lineage in Maharashtra, India, with a particularly successful sublineage giving rise to the Delta VOC. The Delta variant proved even more transmissible and pathogenic than the Alpha variant and ended up superseding all the preexisting variants by mid-2021 (11, 12). In November 2021, a highly divergent VOC called Omicron emerged in South Africa (13). The transmissibility and immune escape capacity of Omicron proved superior to those of all the previous VOC (14, 15), resulting in a worldwide replacement of Delta by Omicron by early 2022. Recent studies point to a lower pathogenicity of the Omicron variant (16), raising the possibility of a shift in SARS-CoV-2 evolution toward viral attenuation.

Several key spike mutations have been shown to play a role in the increased transmissibility or immune escape capacity of the VOC. The initial D614G mutation was shown to increase the infectivity of SARS-CoV-2 in several cell culture systems (3, 17–19). This translated into an increased transmissibility and viral replication capacity in the hamster and ferret models of SARS-CoV-2 infection (20, 21). Structurally, the D614G mutation abrogated an interprotomer contact, which caused the spike receptor binding domain (RBD) to more readily adopt an up conformation, thus facilitating the interactions with the ACE2 receptor (22, 23). Further structural studies showed that D614G also had a key role in stabilizing the noncovalent association of the S1 and S2 spike subunits once they were cleaved, through the ordering of a loop reinforcing intraprotomer interactions (17, 24, 25). Thus, the D614G mutation made the spike more stable but also more prone to interact with its receptor, accounting for the clear selective advantage conferred to the virus.

The N501Y mutation shared by the Alpha, Beta, and Gamma VOC was shown to increase the affinity of the spike for the ACE2 receptor and to be sufficient to increase SARS-CoV-2 infectivity and transmissibility in the hamster model (26). Another group of spike mutations located close to the receptor binding motif and including the E484K, K417N/T, and L452R substitutions are involved in the escape of VOC from neutralizing antibodies (1, 21). A third group of VOC mutations are located in the vicinity of the S1/S2 cleavage site at R685/S686 and may thus influence the processing of the spike. The original SARS-CoV-2 Wuhan strain is characterized by the presence of a polybasic motif, 681-PRRAR-685, just N-terminal to the S1/S2 cleavage site, a feature unique among sarbecoviruses (27, 28). The polybasic motif is recognized by the furin protease during spike export to the surfaces of infected cells, resulting in a partial cleavage of the spike trimers incorporated into virions (29–31). The cleavage at the S1/S2 site preactivates the spike, so that SARS-CoV-2 virions may need only one additional proteolytic cleavage for viral entry (29, 32), resulting in a more fit virus *in vivo* (33, 34). Indeed, when the S1/S2 site is precleaved, the spike bound to the ACE2 receptor requires only

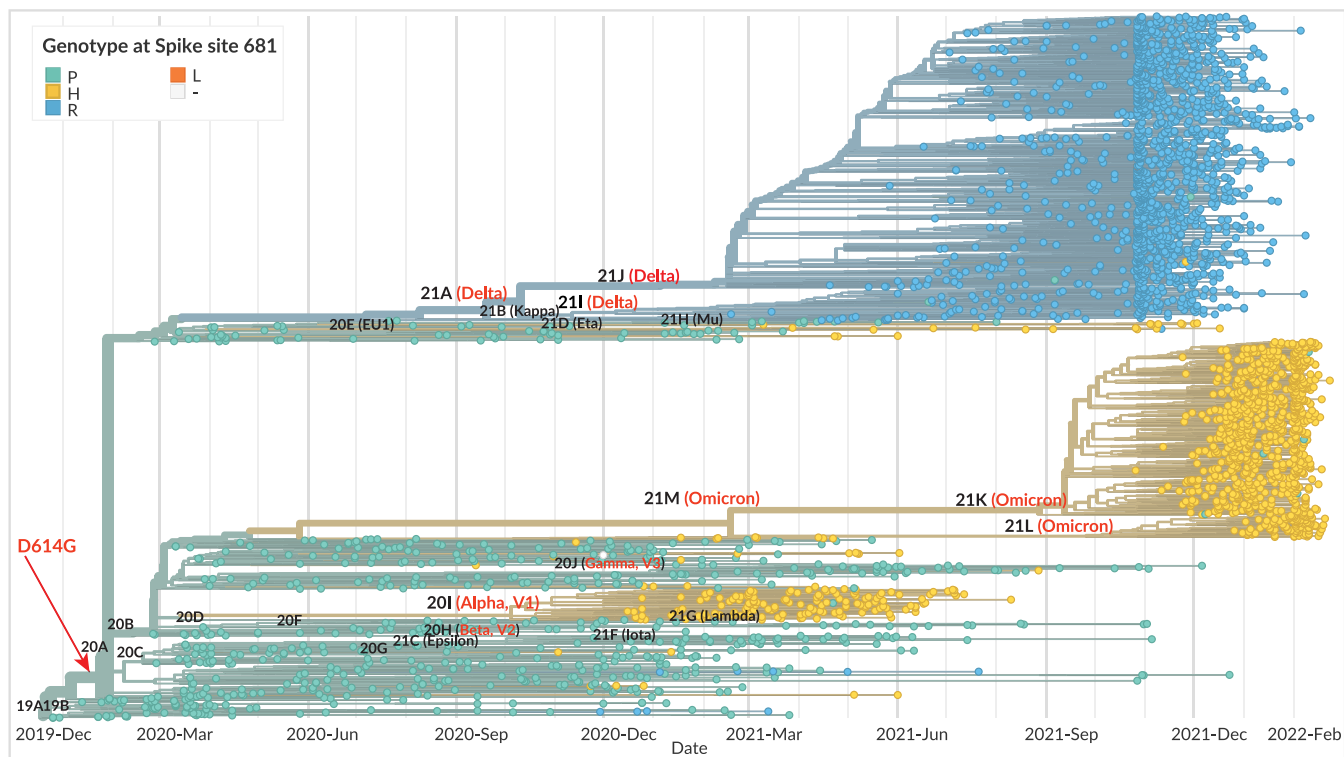


**FIG 1** Phylogeny of SARS-CoV-2 variants, with the spike genotype at position 681 highlighted. The phylogeny is based on 3,247 SARS-CoV-2 genomes sampled globally between December 2019 and February 2022, from the database curated by the GISAID Initiative (<https://www.gisaid.org/>). The phylogenetic tree was generated by the Nextstrain open-source project (<https://nextstrain.org/>), with data points colorized according to spike genotype at position 681 (turquoise, P681; yellow, H681; blue, R681; orange, L681). The branches are labeled with SARS-CoV-2 clades according to the Nextstrain nomenclature, with variant names in parentheses. VOC names are in red. The estimated emergence of the D614G mutation is indicated by a red arrow.

a single cleavage at the S2' site to release the fusion peptide and transition to a fusogenic conformation (35). This additional cleavage may be provided by surface serine proteases such as TMPRSS2 or by endosomal proteases such as cathepsin L if virions are endocytosed (4, 36–39).

Notably, several of the SARS-CoV-2 variants carry a mutation at P681, just upstream of the polybasic S1/S2 cleavage site (Fig. 1). The Alpha and Theta VOI carry a P681H change, which increases the local positive charge and may thus facilitate furin cleavage (40). Indeed, SARS-CoV-2 spikes carrying the P681H mutation were shown to be more cleaved and more fusogenic than their nonmutated counterparts in most (41–43), though not all (44), studies. Of note, the Alpha variant also carries a nearby T716I mutation that may further influence spike cleavage. The Delta variant and the Kappa VOI carry a P681R mutation, which further increases the basic nature of the S1/S2 cleavage motif. This mutation was shown to increase the degree of cleavage at S1/S2, resulting in a spike that is even more fusogenic than that of Alpha (45, 46). The P681R mutation provides a clear competitive advantage to Delta in terms of infectivity in cell culture systems and in animal models of infection (45, 47). More broadly, there has been a consistent trend toward increased S1/S2 cleavage in the different VOC and VOI that emerged in the past 2 years, which may help account for their higher transmissibility and pathogenicity (42). In contrast, the recently emerged Omicron variant shows a low degree of S1/S2 cleavage in virions released in culture, even though it carries the P681H mutation also found in the Alpha spike (14, 48). The limited degree of precleavage reported for the Omicron spike and its preference for the endosomal rather than the TMPRSS2 entry route may contribute to the lower pathogenicity reported for this variant (16, 49).

Phylogenetic analyses suggest that each VOC arose independently, rather than by sequential evolution (Fig. 1). However, it remains intriguing that VOC did not arise prior

to the selective sweep that replaced the original Wuhan strain by the D614G-carrying variant. To address this issue, we assessed possible epistatic interactions between D614G and the dominant S1/S2 cleavage site mutations. Analyses of fusogenic capacity, spike processing, and infectivity of pseudotyped viruses did reveal interactions between these two types of genetic changes. Specifically, the stabilizing effect of the D614G mutation proved necessary to maintain the infectious capacity of virions carrying a highly fusogenic spike, pointing to the critical role of D614G in enabling the emergence of the VOC.

## RESULTS

**Design of spike mutations.** The cleavage site mutations present in the SARS-CoV-2 VOC were introduced into the spike sequence of the reference Wuhan strain (Fig. 2). Specifically, we constructed spike-expressing phCMV vectors carrying the point mutation P681H or T716I, found in the Alpha variant, and P681R, found in the Delta variant (Fig. 2A). Of note, the P681H mutation is also present in the currently emerging Omicron variant. Controls included a Wuhan spike with a deletion of the furin cleavage site (FCS) equivalent to that found in the naturally occurring bat coronavirus RaTG13. This  $\Delta$ FCS mutation corresponded to the deletion of amino acids (aa) 681 to 684 (PRRA), resulting in a TNS/RVA sequence at the S1/S2 junction. To evaluate interactions between the early-occurring D614G mutation and the more recently emerged cleavage site mutations, the Wuhan (wild type [WT]) and cleavage site mutant spikes were constructed in two versions, with or without the D614G mutation (Fig. 2B). As references, we also generated spikes carrying the full complement of mutations present in the Alpha and Delta variants.

**The D614G mutation and the deletion of the furin cleavage site both increase intact spike expression at the cell surface.** Spike-expressing vectors were initially transfected in HEK 293Tn cells (referred to here as HEK cells) to verify that the spike proteins were properly expressed at the cell surface. Transfected cells were labeled with the human monoclonal antibody (MAb) 129, which is known to cross-react with the S1 subunit of the SARS-CoV-2 variants included in the study (43). All of the vectors tested resulted in efficient expression of the spike, with over 70% of HEK cells labeled with MAb 129 (Fig. 3A and B; also, see Fig. S1A in the supplemental material). Analysis of the mean fluorescence intensity (MFI) of transfected HEK cells showed that the  $\Delta$ FCS spike, lacking the FCS, was expressed to higher levels (Fig. 3C), possibly because the S1 subunit could not be shed from the cell surface. The difference in MFI between the WT and  $\Delta$ FCS spikes proved significant only for the versions of the spikes expressing G614. To systematically evaluate the effect of the D614G mutation on spike surface expression, we computed the ratios of MFI for spike pairs carrying G614 or D614 (Fig. 3E). This analysis showed that mean MFI ratios were above 1, suggesting that G614 increased spike surface expression. The MFI ratio was significantly higher for WT spikes than P681R spikes, suggesting that the D614 effect was modulated by spike cleavage. Similar trends were observed when analyzing the G614/D614 ratios of the percentage of spike-expressing cells (Fig. 3D), though the difference between WT and P681R did not reach significance. Overall, this analysis showed that both the FCS deletion and the D614G mutation promoted the expression of S1-containing spikes at the cell surface.

Analysis of spike expression with an S1-specific antibody, as described above, quantitates only "intact" spikes that have not shed the S1 subunit and retain a fusogenic capacity. To evaluate the expression of all the spike proteins that reach the cell surface, independent of S1 shedding, we labeled the spike-transfected cells with an S2-specific monoclonal antibody (GTX-S2). Analysis of the percent S2-positive cells showed equivalent expression of all the spike proteins tested (Fig. S2A). This finding was confirmed by performing surface staining with MAb 10-S2, a second S2-specific monoclonal antibody (Fig. S2B). Thus, the increase in spike surface expression associated with the FCS deletion and the D614G mutation concerned only S1-containing intact spikes, not the total spike content. These observations were compatible with an abrogation of S1 shedding by the FCS deletion and a limitation of S1 shedding by the D614G mutation,

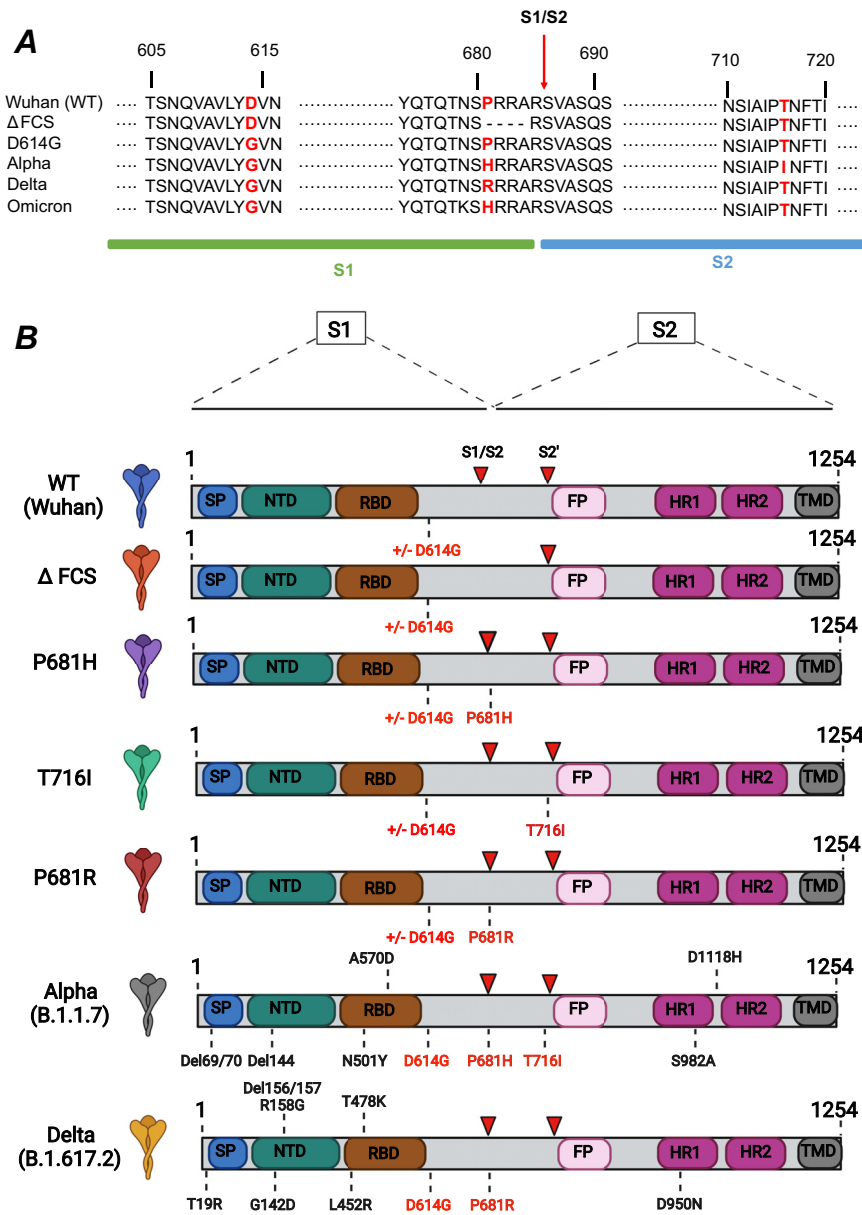


**FIG 2** Spike mutations analyzed in the present study. (A) Sequences surrounding the spike mutations studied. The S1/S2 spike cleavage site is indicated by a vertical arrow. The mutations studied are highlighted in red. The ΔFCS mutation corresponds to the deletion of the PRRA sequence at the S1/S2 cleavage site. (B) Schematic of the spike expression vectors used in the present study. The mutations ΔFCS, P681H, P681R, and T716I were inserted into the Wuhan WT spike backbone truncated at residue 1254, in the presence or absence of the D614G mutation. The spikes containing the full complement of mutations present in the Alpha and Delta VOC were used as controls. SP, signal peptide; NTD, N-terminal domain; RBD, receptor binding domain; FP, fusion peptide; HR, heptad repeat; TMD, transmembrane domain. Red arrowheads indicate the S1/S2 and S2' cleavage sites.

consistent with the literature (17–19, 24, 25). Further analyses of the fluorescence intensity of the S2 subunit showed a trend toward the D614G mutation in decreasing S2 surface expression (Fig. S2C and D). This observation was confirmed by an analysis of the G614/D614 ratios for S2 expression, which were below 1 for all the spike pairs tested (Fig. S2E to H). The moderate decrease in S2 surface expression induced by the D614G mutation may result from altered spike trafficking. Alternatively, the mutation may decrease accessibility of S2 to monoclonal antibodies due to conformational changes or increased S1 content. Overall, D614G induced an apparent decrease in total

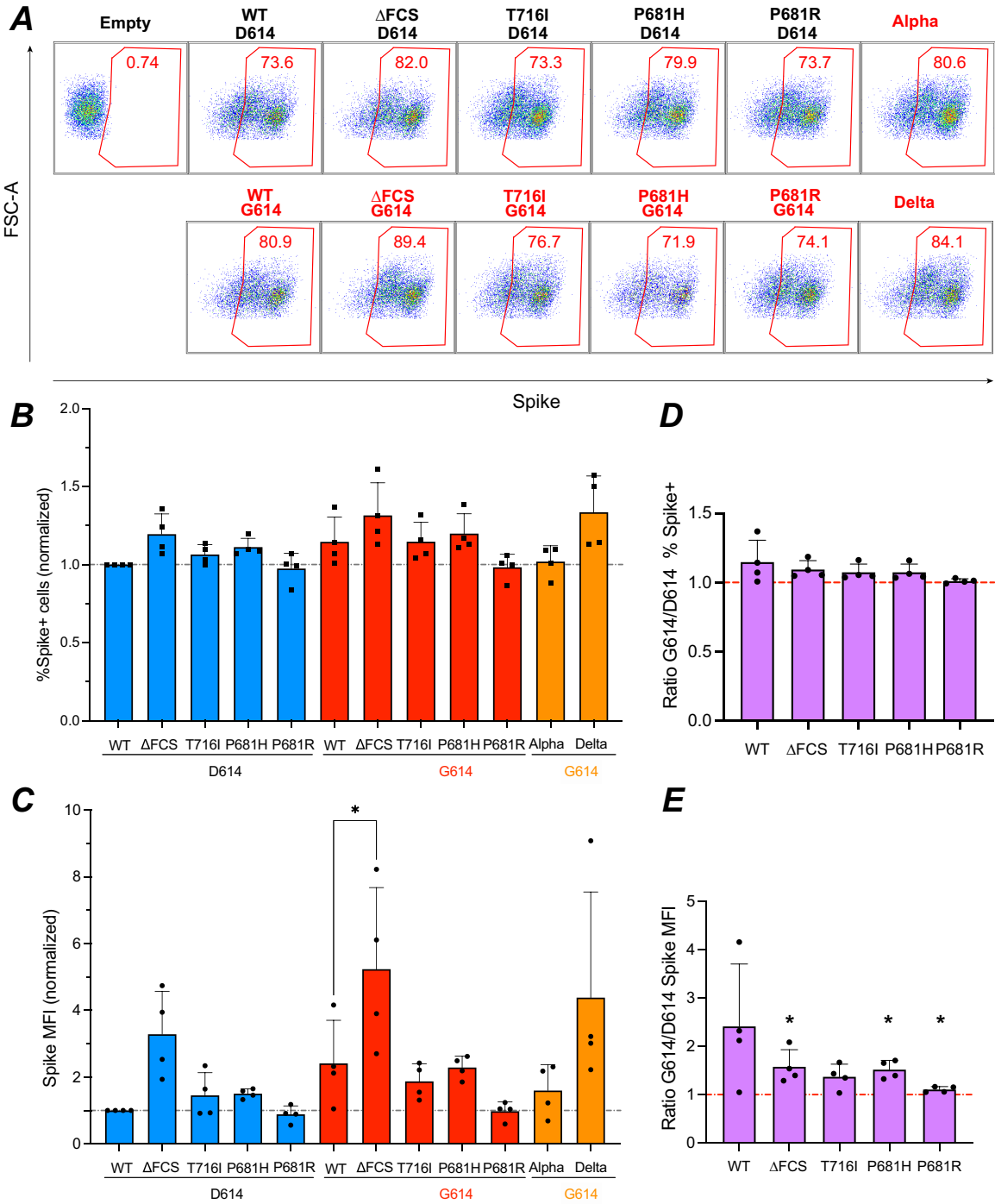


**FIG 3** Increased spike surface expression upon deletion of the furin cleavage site. (A) Representative examples of spike surface expression. HEK 293T cells were transfected with spike expression vectors and analyzed by flow cytometry after surface staining with the spike-specific human MAb 129. The percentage of spike-positive cells in live cells is reported. (B and C) The percentage of spike-positive cells (B) and MFI of spike in live cells (C) normalized to the WT value are reported. Statistics were measured by one-way ANOVA, with the Holm-Šidák correction for multiple comparisons. D614 backbone mutants were compared to the WT D614 spike, while G614 backbone mutants were compared to the WT G614 spike. (D and E) Ratio of spike surface expression measured in the G614 backbone to that in the D614 backbone, using either the percentage (D) or the MFI (E) of spike-positive cells for measurement. Statistics evaluating whether each ratio is different from 1 were measured by one-sample *t* tests. (B to E) Means and standard deviations (SD) are shown for 4 independent experiments. \*, *P* < 0.05.

spike surface expression, which was largely compensated for by an increase in intact spike content.

**The P681H/R mutations increase SARS-CoV-2 spike fusogenicity.** The fusogenic capacity of the different spikes was evaluated in a green fluorescent protein (GFP) split system where spike-transfected HEK cells expressing the truncated reporter protein GFP1-10 were mixed with Vero-E6 cells expressing the complementary reporter protein GFP11 (50, 51). Upon cellular fusion, reconstitution of a functional GFP due to GFP1-10–GFP11 interaction resulted in fluorescent emission at 488 nm (Fig. 4A). GFP<sup>+</sup> syncytia were visualized on an Opera imaging system, and the GFP<sup>+</sup> surface normalized to the number of nuclei was quantified by automated image analysis.

The  $\Delta$ FCS spike did not induce detectable fusion (Fig. 4B), compatible with the notion that cleavage at the FCS is required for SARS-CoV-2 spike-dependent fusion at the cell surface. In contrast, all of the other spikes induced the formation of GFP<sup>+</sup> syncytia, with syncytia appearing larger for spikes carrying the P681H/R mutations (Fig. 4B). Quantitative image analysis showed that the WT and T716I spikes had equivalent fusogenic capacity (Fig. 4C). In contrast, the P681H and P681R spikes induced significantly more fusion than the WT spike ( $P < 0.0001$  in the presence of D614;  $P < 0.01$  in the presence of G614), consistent with previous findings by us and others (42, 43). The Delta spikes also proved strongly fusogenic, compatible with the presence of the P681R mutation (11).

Comparison of fusion achieved in presence and absence of the D614G mutation was measured by fusion ratios (Fig. 4D). This analysis showed that the D614G mutation increased the fusogenicity of the WT Wuhan and T716I spikes, with ratios of  $\geq 1$ , possibly due to increased spike expression at the cell surface. In contrast, the D614G effect was weak or absent for the already highly fusogenic spikes carrying P681H/R mutations.

**Cleavage site mutations limit spike incorporation into pseudoviruses.** Pseudotyped viruses (PV) were produced by cotransfecting HEK cells with a SARS-CoV-2 spike expression vector, a GFP-lentivector backbone, and HIV-derived packaging plasmids. PV particles concentrated by ultracentrifugation were analyzed for spike incorporation and processing by Western blotting. Dual labeling was obtained with a polyclonal anti-S1 antibody (green fluorescence) and a monoclonal anti-S2 antibody (red fluorescence), so that the uncleaved spike precursor, S0, containing both the S1 and S2 subunits appeared yellow (Fig. 5A, top). PV protein extracts were normalized according to their content in HIV p24 capsid protein (Fig. 5A, bottom).

Particle pseudotyped with the  $\Delta$ FCS spike showed a highly predominant S0 band, as expected for a spike devoid of an S1/S2 cleavage site. In contrast, S1 and S2 subunits were detected in PV expressing a spike with an FCS. To evaluate the total amount of spike incorporated by the different PV, we measured the summed intensities of the S2 and S0 bands (in the red channel), relative to the amount of p24 capsid protein (Fig. 5B). Of note, the (S0+S2)/p24 parameter takes into account all the spike moieties incorporated into the PV, irrespective of their cleavage status or of the possible shedding of the S1 subunit. Quantitation of this parameter showed that all of the cleavage site mutations tended to decrease total spike incorporation, with an effect that was more marked for the T716I mutant. The Alpha PV also showed low spike incorporation compared to the WT G614 PV. Based on a G614/D614 ratio analysis (Fig. 5C), the D614G mutation had minimal effect on total spike incorporation, except for a possible decrease in incorporation of the P681R spike.

**The D614G mutation promotes spike cleavage but limits S1 shedding.** We then analyzed the ratio of S2 subunit to S0 precursor, in order to evaluate the extent of spike cleavage in PV particles. This analysis showed that the P681H/R mutations strongly promoted spike cleavage (Fig. 5D), consistent with the literature (41, 42, 45, 46). The Delta PV also harbored almost fully cleaved spikes, while this was not apparent for the Alpha PV, suggesting that other mutations such as T716I counterbalanced the procleavage effect of P681H. The G614/D614 ratio analysis showed that the presence of the G614 mutation increased spike cleavage in the WT and T716I PV but had no discernible effect on the already highly cleaved spikes of the P681H and P681R PV (Fig. 5E).

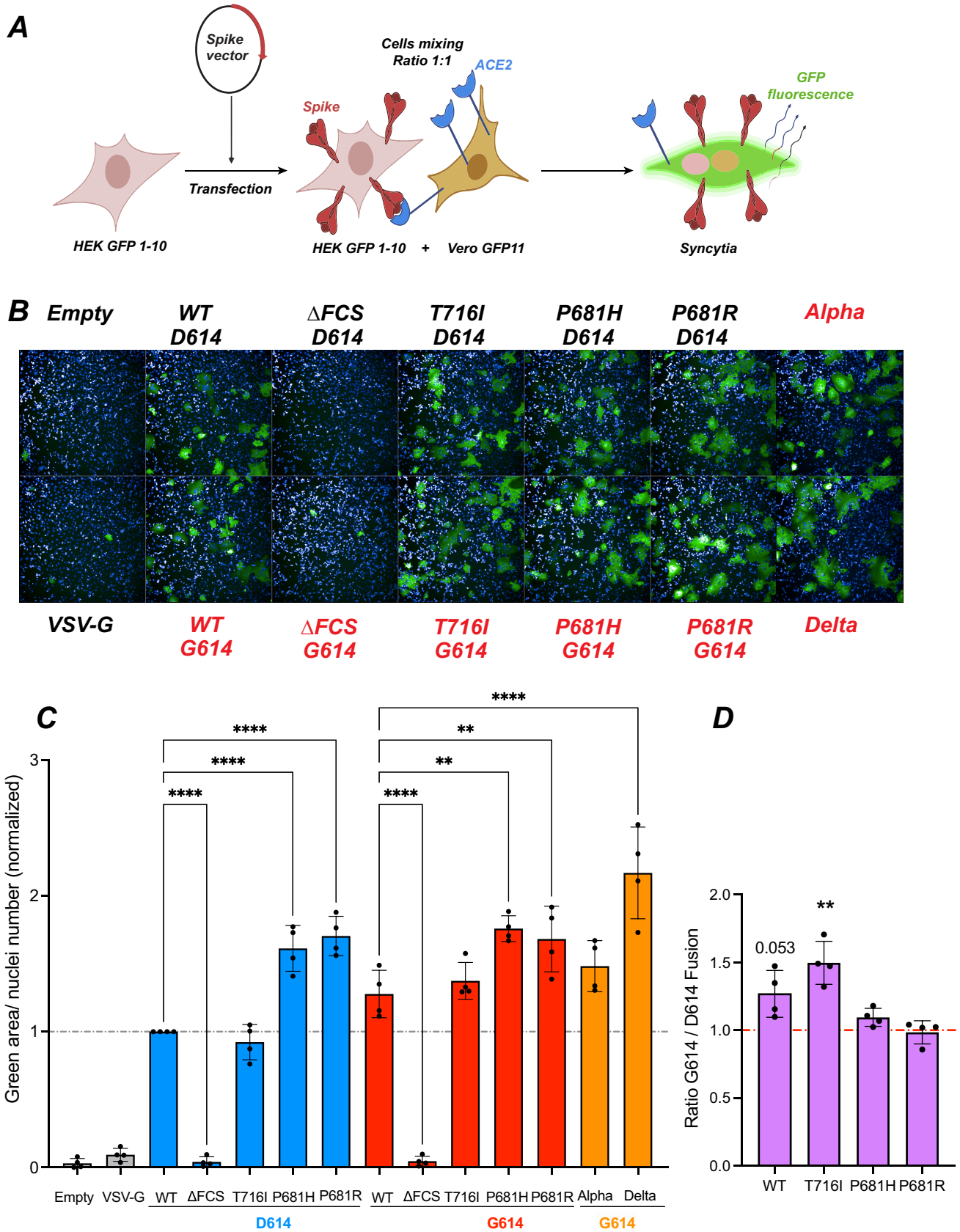


**FIG 4** The P681H/R mutations increase spike fusogenicity. (A) Principle of the cell-cell fusion assay. HEK GFP1-10 are transfected with spike vectors and then mixed with Vero GFP11 at a 1:1 ratio. Spike-ACE2 interactions lead to cell-cell fusion. Upon syncytium formation, complementation between the (Continued on next page)



The relative amount of S1 subunit retained on the different PV was then measured by quantifying the S1/S2 ratio (Fig. 5F). The T716I mutation was associated with a very low S1/S2 ratio relative to WT, while the P681H/R mutations did not have a marked effect on the S1/S2 ratio. Thus, the T716I mutation induced marked S1 shedding, while the addition of a basic amino acid in the FCS appeared neutral for shedding, even though it increased spike cleavage. The presence of the D614G mutation promoted S1 retention in all the PV tested, as shown by values above 2 in the G614/D614 ratio analysis relative to the S1/S2 parameter (Fig. 5G). In particular, D614G efficiently corrected the deleterious effect of T716I on S1 shedding. Taken together, these results show that the D614G mutation promoted spike cleavage but limited S1 shedding, consistent with the literature (17–19, 24, 25). Presence of D614G thus enabled the production of viral particles with a high content of cleaved spike.

A Western blot analysis was also carried out on lysates of HEK cells used to produce the PV particles (Fig. S3). More spikes remained in an uncleaved S0 state in producer cells than in PV, likely because a fraction of cellular spikes had not yet completed their maturation. Nevertheless, the parameters that measured spike content [(S0+S2)/actin], spike cleavage (S2/S0), and S1 shedding (S1/S2) showed patterns similar to those observed in PV, indicating that the studied spike mutations already exerted their effects at the level of producer cells. One exception was the lower cleavage of the spike carrying both the P681R and D614G mutations compared to the D614G-carrying WT spike in producer cells (Fig. S3C). The reverse trend was observed in PV (Fig. 5D), suggesting that spikes carrying P681R could be further cleaved after viral budding.

**The D614G mutation preferentially increases the infectivity of P681H/R-carrying pseudoviruses.** To evaluate the impact of spike mutations on viral infectivity, we measured the extent of single-cycle infection induced by PV on HEK cells expressing the ACE2 receptor, in the presence or absence of the TMPRSS2-activating protease (Fig. S1B). At 48 h, the infection was evaluated by the percentage of target cells expressing the GFP reporter gene, after transfer by the pseudotyped lentivector added at a dose of 0.125  $\mu\text{g}$  p24 (representative examples in Fig. 6A and Fig. S4; quantitation in Fig. 6B). This analysis showed that, in the absence of the D614G change, the infectivity of PV carrying the cleavage site mutations T716I and P681H/R was low compared to that of the WT (Fig. 6B). In contrast, the  $\Delta\text{FCS}$  spike conferred high infectivity in HEK-ACE2 cells, confirming that an FCS was not required for viral entry in these cells (18, 31, 33). A dose response analysis supported these findings at different viral input doses (Fig. S5). Infectivity was overall higher in HEK-ACE2-TMPRSS2 than HEK-ACE2 cells (Fig. S5A). Differences in infectivity between the PV were less marked than in HEK-ACE2 cells (Fig. 6B and C), suggesting that an additional entry route enabled by the TMPRSS2 protease could attenuate mutant-induced entry defects.

The G614/D614 infectivity ratios were then computed for all the lentivector doses tested (Fig. 6D and E), including the 0.125- $\mu\text{g}$  dose shown in Fig. 6B and C. Analysis of these ratios showed that the D614G mutation increased infectivity of the WT and P681H PV in HEK-ACE2, as indicated by ratios significantly above 1 for the 0.125- $\mu\text{g}$  dose ( $P < 0.05$ ) (Fig. 6D). A trend for increased infectivity was also observed for the P681R PV carrying D614G at all doses tested. In contrast, infectivity of the T716I PV remained unchanged and that of the  $\Delta\text{FCS}$  PV was significantly decreased in the presence of the D614G mutation (Fig. 6D). A degree of cytotoxicity was observed at the highest PV input dose (0.5  $\mu\text{g}$ ) (Fig. S5B), which may have affected the measurement

#### FIG 4 Legend (Continued)

GFP1-10 and GFP11 fragments generates functional GFP, resulting in a fluorescent emission. (B) Representative images of a fusion assay monitored at 18 h after spike transfection. Cell nuclei were stained with DAPI (blue), while syncytia were detected by GFP fluorescent emission (green). The spike vectors used are shown, with those containing the D614G mutation in red. (C) Quantification of cell-cell fusion induced upon spike expression. The green fluorescent area divided by the number of nuclei is reported, with normalization to the WT spike condition. Statistics were measured by one-way ANOVA, with the Holm-Šidák correction for multiple comparisons. D614 backbone mutants were compared to the WT D614 spike, while G614 backbone mutants were compared to the WT G614 spike. (D) Ratios of cell-cell fusion measured for spikes in the G614 backbone to that in the D614 backbone. Statistics evaluating whether each ratio is different from 1 were measured by one-sample *t* tests. (C and D) Means and SD are shown for 4 independent experiments. Each dot represents the mean of technical triplicate measurements. \*\*,  $P < 0.01$ ; \*\*\*\*,  $P < 0.0001$ .

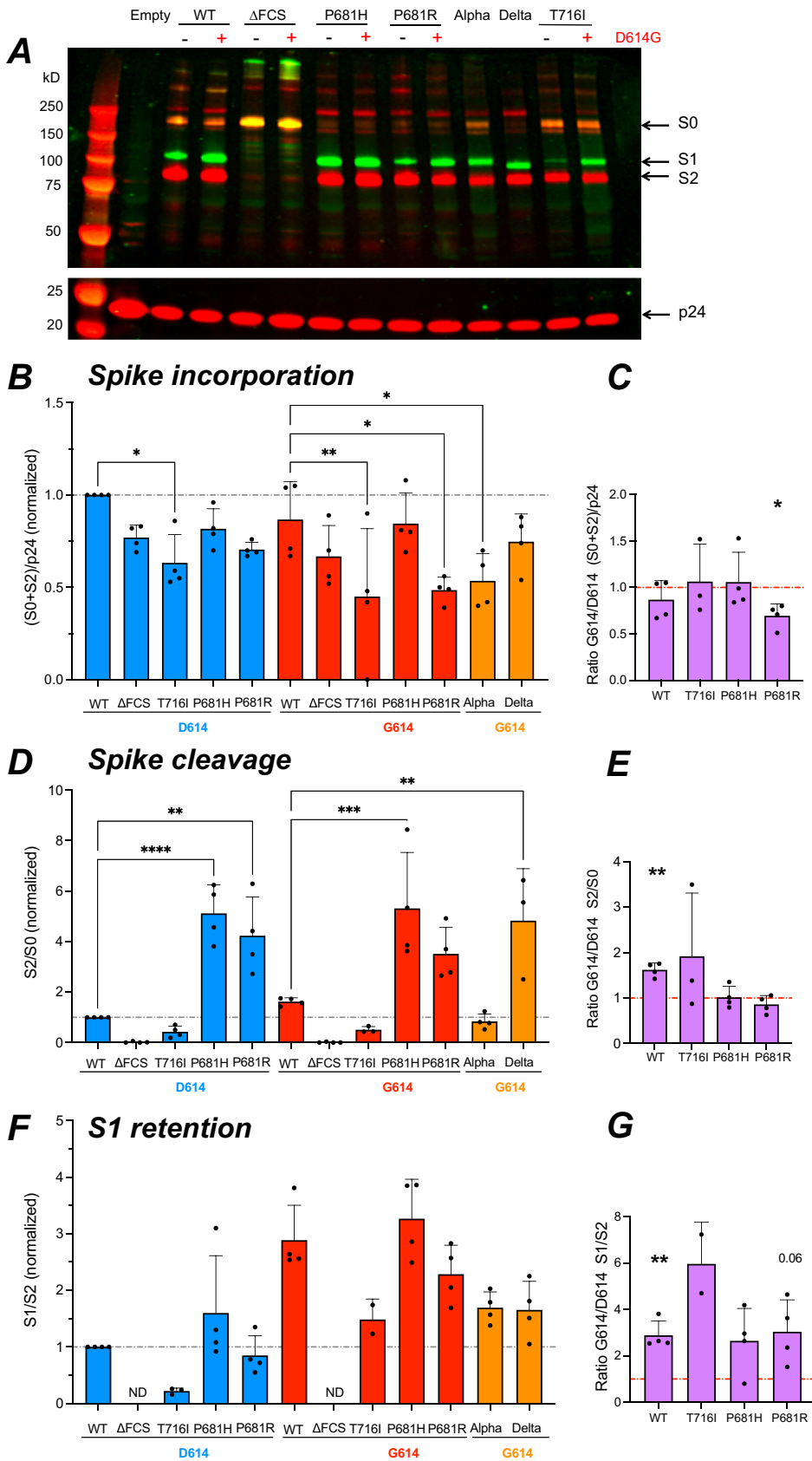


**FIG 5** The D614G mutation promotes S1 subunit retention in virions. The different forms of spike present into PV were analyzed by Western blotting on concentrated PV particles. (A) Representative Western blot (Continued on next page)

of infectivity ratios at this dose (gray bars in Fig. 6D and E). Interestingly, the effect of D614G appeared more marked for the PV carrying the basic P681R/H mutations than for the WT, as shown by ratios of  $\geq 2$  (Fig. 6D, red line), suggesting that D614G may have played a compensatory role that was important in the emergence of the P681H/R-carrying variants. The Alpha PV retained relatively low infectivity in HEK-ACE2 cells (Fig. 6B), suggesting that mutations other than D614G and P681H also impacted viral entry, with a possible negative role of T716I. The effect of D614G was less apparent in HEK-ACE2-TMPRSS2 than in HEK-ACE2 cells but remained more marked for the P681R/H than the WT PV (Fig. 6C and E), confirming that D614G preferentially increased the infectivity of PV carrying the P681H/R basic mutations.

**The D614G mutation increases infectivity in different cellular contexts.** To test the generality of these findings, we measured the infectivity of PV in the osteosarcoma cell line U2OS-ACE2 with and without TMPRSS2 and in the lung adenocarcinoma cell line Calu-3. As PV expressing a GFP reporter gene gave a low detection signal in these cell lines, we switched to a PV system where the backbone lentivector expressed luciferase, resulting in a higher signal-to-noise ratio (Fig. 7). The pattern of infectivity observed in U2OS-ACE2 was similar to that observed in HEK-ACE2, with a relative defect of the T716I, P681H, and P681R PV compared to WT and a highly efficient entry of the  $\Delta$ FCS PV (Fig. 7A). The D614G mutation markedly increased PV infectivity in U2OS-ACE2 cells (Fig. 7B), with a partial restoration of infectivity for the P681H/R mutants. The Alpha PV showed an infectivity equivalent to that of WT-G614, while that of the Delta PV proved significantly higher (Fig. 7A).

Analyses in U2OS-ACE2-TMPRSS2 showed that the presence of TMPRSS2 led to an overall increase in PV infectivity (Fig. 7C). The relative differences in PV infectivity showed a pattern similar to that observed in the absence of TMPRSS2, except that the Delta PV showed an infectivity comparable to rather than higher than that of the WT. The presence of the D614G mutation led to a full restoration of infectivity for the P681H PV and to a partial restoration for the P681R PV (Fig. 7C and D).

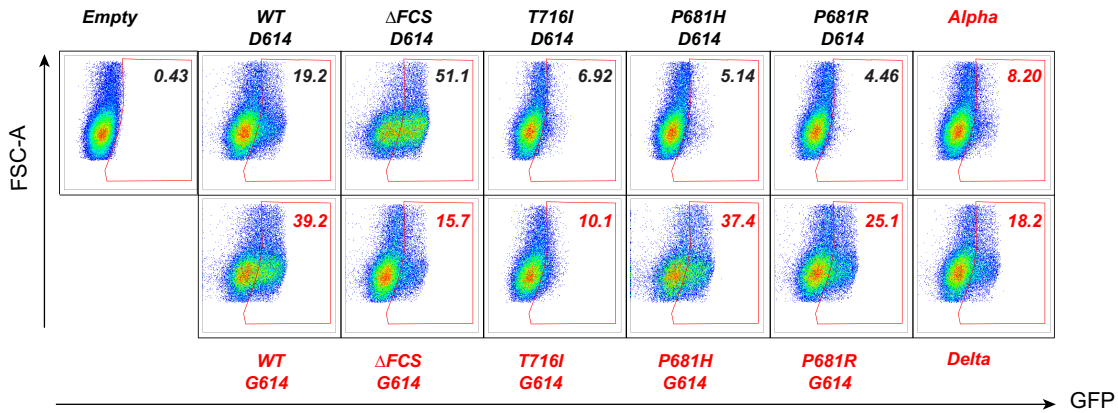
In the Calu-3 cell line, which expresses ACE2 and TMPRSS2 endogenously (37), PV entry was lower than in cell lines transduced with the ACE2 and TMPRSS2 genes (Fig. 7E). The  $\Delta$ FCS PV showed drastically decreased infectivity in Calu-3, confirming that a functional FCS was required for efficient entry in this cell line (29, 32, 33). The T716I PV still showed a decreased infectivity compared to WT, while the P681H/R PV were as infectious as WT in the Calu-3 setting. The Alpha PV also showed an infectivity comparable to that of WT-G614, while infectivity of the Delta PV was significantly increased (Fig. 7E).

The G614/D614 infectivity ratios were above 1 for all the PV tested (Fig. 7F), indicating that the D614G mutation increased infectivity in Calu-3 cells, though this increase appeared moderate compared to that seen in other cell lines. Concerning the P681R/H mutants, the infectivity ratios were in the 1.5-to-2.5 range in Calu-3, while they were in the 3-to-7 range in HEK-ACE2 and U2OS-ACE2 with and without TMPRSS2, suggesting that the compensatory effect of the D614G mutation depended on the cellular context.

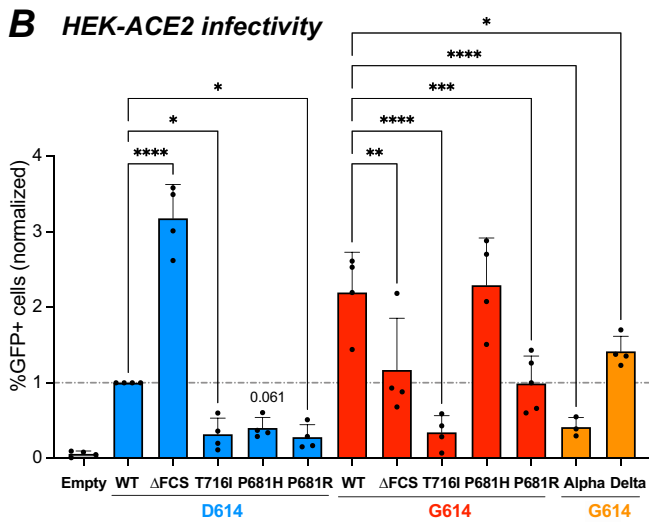
#### FIG 5 Legend (Continued)

showing the S1 (green) and S2 (red) spike subunits (top) and the p24 Gag protein (red) used for normalization (bottom). The equivalent of 300 ng p24 was loaded in each lane. Molecular weight markers were loaded in the first lane, with the expected marker size indicated on the left. The uncleaved spike precursor S0 is visible in yellow due to the superposition of green and red fluorescence. (B) Quantitation of total spike incorporated (S0 + S2), relative to p24 content, and normalized to the WT value. The fluorescence intensity of each band was quantified with the Image Studio Lite software. (C) Ratio of total spike incorporated measured in the G614 backbone to that in the D614 backbone. (D) Quantitation of total cleaved spike, measured by the S2/S0 ratio and normalized to the WT value. (E) Ratio of total cleaved spike measured in the G614 backbone to that in the D614 backbone. (F) Quantitation of S1 subunit retention in PV particles, measured by the S1/S2 ratio, and normalized to the WT value. ND, not detectable. (G) Ratio of S1 retention in the G614 backbone to that in the D614 backbone. (B, D, and F) Statistics were measured by one-way ANOVA, with the Holm-Šidák correction for multiple comparisons. D614 backbone mutants were compared to the WT D614 spike, while G614 backbone mutants were compared to the WT G614 spike. (C, E, and G) Statistics evaluating whether each ratio was different from 1 were measured by one-sample *t* tests. (B to G) Means and SD are shown for  $\geq 3$  independent experiments, except for T716I S1 retention, where  $n = 2$ . \*,  $P < 0.05$ ; \*\*,  $P < 0.01$ ; \*\*\*,  $P < 0.001$ ; \*\*\*\*,  $P < 0.0001$ .

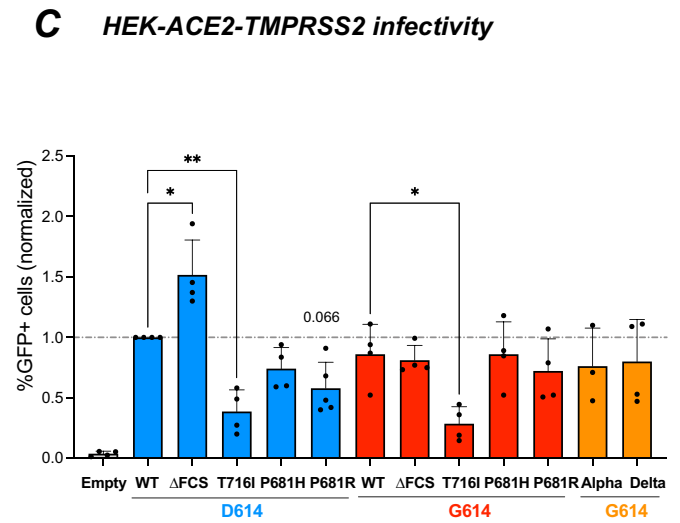
**A HEK-ACE2**



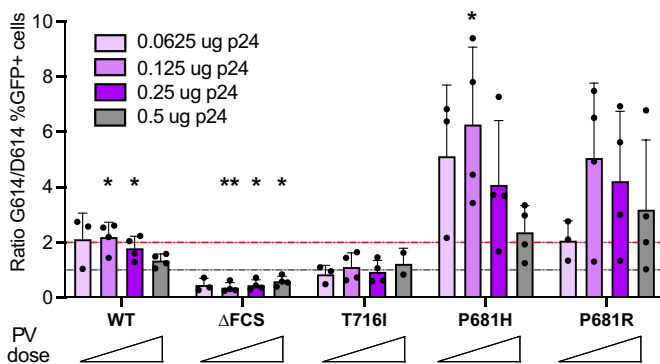
**B HEK-ACE2 infectivity**



**C HEK-ACE2-TMPRSS2 infectivity**



**D HEK-ACE2 G614/D614 ratio**



**E HEK-ACE2-TMPRSS2 G614/D614 ratio**

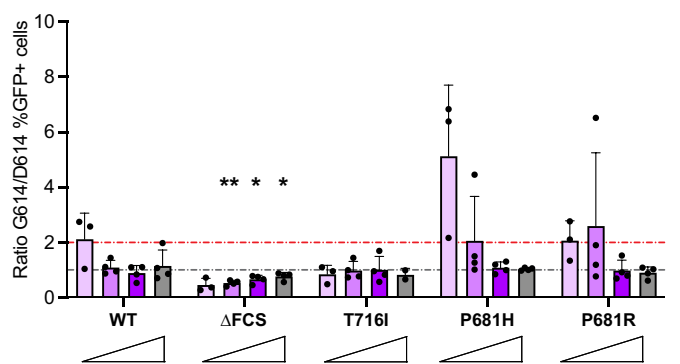
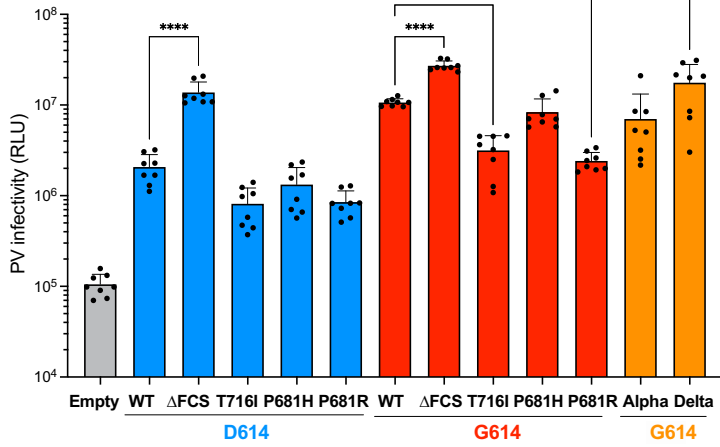
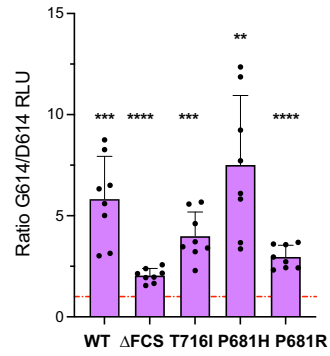


**FIG 6** The D614G mutation preferentially increases the infectivity of P681H/R-carrying pseudoviruses. The infectivity of GFP lentivector pseudotyped with the different spikes was analyzed in HEK-ACE2 cells that were induced for TMPRSS2 expression or uninduced. (A) Representative infection experiment in HEK-ACE2 cells. Cells were inoculated with 0.25  $\mu$ g of p24 equivalent. The infectivity of PV is measured by the percentage of GFP<sup>+</sup> cells, reported in the top right corner of each plot. (B and C) Quantitation of PV infectivity at the intermediate PV dose corresponding to the 0.125  $\mu$ g of p24 equivalent. The percentage of GFP<sup>+</sup> cells obtained in HEK-ACE2 cells (B) and HEK-ACE2-TMPRSS2 cells (C) normalized to the WT value is reported. Statistics were measured by one-way ANOVA, with the Holm-Šidák correction for multiple comparisons. D614 backbone mutants were compared to the WT D614 spike, while G614 backbone mutants were compared to the WT G614 spike. Means and SD are shown for  $\geq 3$  independent experiments. (D and E) Ratio of PV infectivity in HEK-ACE2 (D) and in HEK-ACE2-TMPRSS2 (E) for spikes in the G614 backbone to that for spikes in the D614 backbone. The ratio was computed for increasing doses of PV ranging from 0.0625 to 0.5  $\mu$ g pf p24 equivalent. The preferential effect of the D614G mutation on the infectivity of PV carrying the P681H/R mutation is evidenced by ratios above 2 (red line, ratio = 2; gray line, ratio = 1). Means and SD are shown for  $\geq 3$  independent experiments, except for the T716I mutant at the highest dose, where  $n = 2$ . Statistics evaluating whether each ratio was different from 1 were measured by one-sample  $t$  tests. \*,  $P < 0.05$ ; \*\*,  $P < 0.01$ ; \*\*\*,  $P < 0.001$ ; \*\*\*\*,  $P < 0.0001$ .

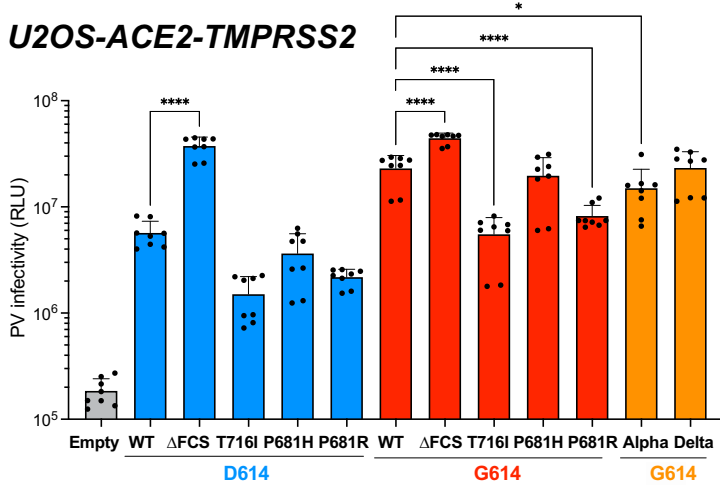
**A U2OS-ACE2**



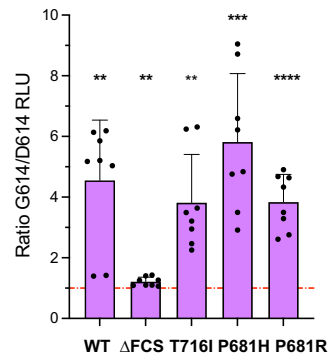
**B**



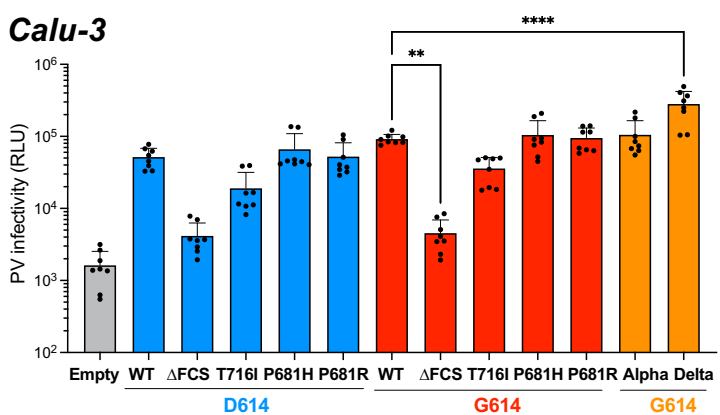
**C U2OS-ACE2-TMPRSS2**



**D**



**E Calu-3**



**F**

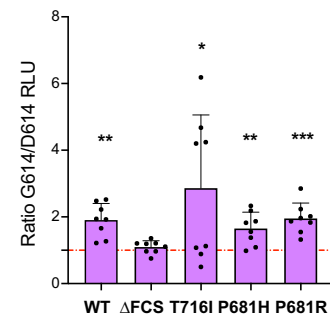


**FIG 7** The D614G mutation increases infectivity in different cellular contexts. The infectivity of Luc lentivector pseudotyped with the different spikes was analyzed in different cell lines. (A to D) Luciferase activity in U2OS-ACE2 cells (A and B) and U2OS-ACE2-TMPRSS2 cells (C and D) infected with 0.125  $\mu$ g pf p24 equivalent. (E and F) Luciferase activity in Calu-3 cells infected with 1  $\mu$ g pf p24 equivalent. (A, C, and E) Statistics were measured by one-way ANOVA, with the Holm-Šidák correction for multiple comparisons. D614 backbone mutants were compared to the WT D614 spike, while G614 backbone mutants were compared to the WT G614 spike. (B, D, and F) Ratio of PV infectivity in U2OS-ACE2 (B), U2OS-ACE2-TMPRSS2 (D), and Calu-3 (F) cells for spikes in the G614 backbone to that in the D614 backbone. Statistics evaluating whether each ratio is different from 1 were measured by one-sample *t* tests. (A to F) Means and SD are shown for 4 independent experiments, with 2 technical replicates per experiment. \*, *P* < 0.05; \*\*, *P* < 0.01; \*\*\*, *P* < 0.001; \*\*\*\*, *P* < 0.0001.

**Limited effect of the D614G mutation on entry pathway usage.** SARS-CoV-2 is known to use different entry pathways depending on the availability of the proteases involved in spike processing. Specifically, expression of TMPRSS2 promotes entry at the cell surface, while in the absence of this protease, viral entry can take place in endosomes after spike processing via cathepsins B and L (4, 36, 37). As we noted a variable compensatory effect of the D614G mutation depending on the target cell type, we asked whether D614G influenced entry pathway usage. To investigate this, target cells were pretreated with the serine protease inhibitor camostat, which blocks TMPRSS2 activity, and/or with the cysteine protease inhibitor E64D, which blocks the activity of the endosomal cathepsins B and L (36). Pretreated cells were then infected and cultivated in the presence of the inhibitors for 2 days before the inhibition of PV infectivity was measured by luciferase activity.

Viral entry into HEK-ACE2 cells was inhibited at 80% by E64D treatment for most PV tested (Fig. 8A, green line in radar plot) while the blocking effect of camostat was minimal (20%) (Fig. 8A, blue line), suggesting that the endosomal entry route predominated in this cell line (see Fig. S6A for raw infectivity data). The combination of E64D and camostat (Fig. 8A, red line) resulted in inhibition equivalent to that seen with E64D alone, reinforcing the notion of a predominantly endosomal entry. Entry inhibition did not vary depending on the presence or absence of the D614G mutation, suggesting that spike stability was not the main parameter determining the viral entry route. The Delta PV was characterized by a lower susceptibility to entry blocking by the two protease inhibitors, possibly due to the high fusogenicity of the Delta spike. Another exception was the T716I PV carrying the D614G mutation, which showed only 60% inhibition by E64D treatment. However, this resistance was only relative, as this PV retained an overall low infectivity in HEK-ACE2 compared to the other PV carrying D614G (Fig. S6A).

Analysis of entry inhibition in HEK-ACE2-TMPRSS2 showed an inverted pattern compared to that seen in HEK-ACE2, with about 80% inhibition by camostat, and a negligible effect of E64D (Fig. 8B). Thus, the expression of TMPRSS2 was sufficient to switch entry pathways, with the surface route becoming predominant. The Delta PV proved again less susceptible to entry inhibition. The other PV that showed low (40%) entry inhibition by camostat was the  $\Delta$ FCS PV, consistent with the limited capacity of an uncleaved spike to promote surface entry (36). The  $\Delta$ FCS PV were the only ones to show a degree of inhibition by E64D in HEK-ACE2-TMPRSS2, suggesting that limited access to the endosomal route remained available in the presence of TMPRSS2. The presence of the D614G mutation had little or no effect on susceptibility to protease inhibitors, suggesting that the main determinants of entry pathway usage lay with the host cell rather than with the viral particle.

Evaluation of entry inhibition in Calu-3 cells yielded a pattern that was overall similar to that seen in HEK-ACE2-TMPRSS2, compatible with a predominant use of the surface entry route in both cell lines (Fig. 8C and Fig. S6C). Camostat proved highly efficient at blocking viral entry in Calu-3, consistent with a requirement for TMPRSS2 or related serine proteases for viral entry in this cell line (19, 29, 36, 37, 39). Entry inhibition percentages upon camostat treatment were above 80% for most PV, and no further increase in inhibition was seen when E64D was added to camostat. The exception was again the  $\Delta$ FCS PV, which were not inhibited by camostat. However, entry of the  $\Delta$ FCS PV was only marginally higher than that seen for the control PV devoid of spike (Fig. S6C, Empty), confirming that a spike devoid of the FCS enabled only minimal entry in Calu-3 cells (29, 32, 33).

**Partial inhibition of infectivity by combined TMPRSS2 and cathepsin inhibitors in U2OS cells.** The entry inhibition pattern seen in U2OS-ACE2 cells proved intermediate, with neither camostat nor E64D achieving efficient blocking of viral entry in this cell line (Fig. 8D and E and Fig. S6D and E). The inhibition induced by E64D was in the 20-to-40% range, except for  $\Delta$ FCS PV, which remained cathepsin dependent for viral entry. We noted that PV carrying G614 tended to be more susceptible to E64D inhibition than their D614 counterparts, suggesting that PV with stabilized spikes may still partially use the endosomal entry pathway in the U2OS cellular context. Camostat did not inhibit viral entry in U2OS-ACE2 and, intriguingly, also showed a limited effect (about 20% inhibition) in U2OS-

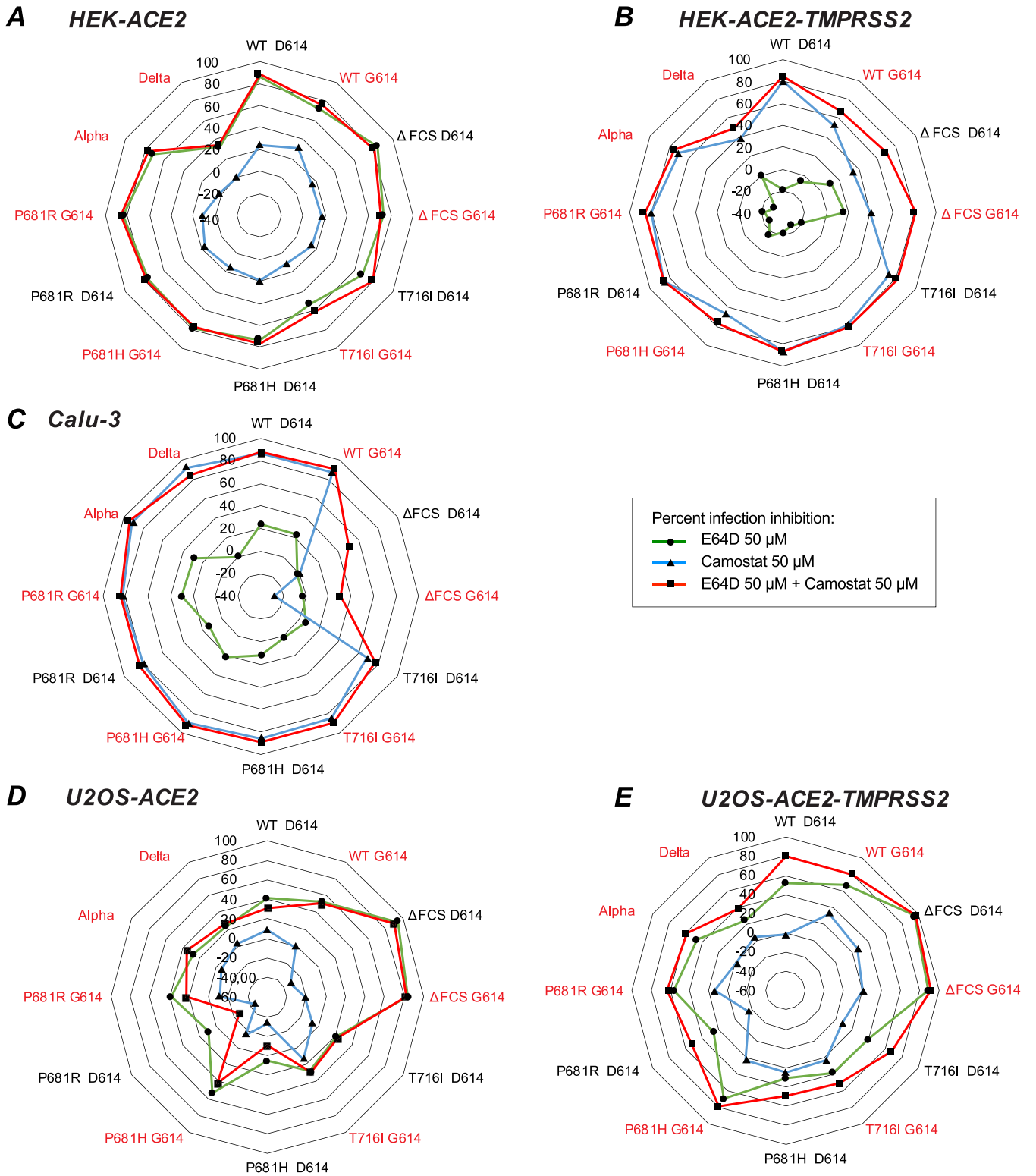


**FIG 8** Partial inhibition of infectivity by combined TMPRSS2 and cathepsin inhibitors in U2OS cells. The TMPRSS2 inhibitor camostat and the cathepsin inhibitor E64D were evaluated for their capacity to block PV infectivity, alone or in combination. The percent infectivity inhibition was measured by the mean decrease in luciferase activity for 3 independent experiments, with 2 technical replicates per experiment:  $[1 - (RLU\ treated/RLU\ untreated)] \times 100$ . The percent infectivity inhibition is reported in radar plots for camostat (blue line), E64D (green line), or the combination of the two inhibitors (red line) in HEK-ACE2 (A), HEK-ACE2-TMPRSS2 (B), Calu-3 (C), U2OS-ACE2 (D), and U2OS-ACE2-TMPRSS2 (E) cells. The names of PV carrying the D614G mutation are in red.

ACE2-TMPRSS2 (Fig. 8E). In contrast, the inhibitory effect of E64D was maintained and even at times increased (range, 20 to 60%) in the presence of TMPRSS2. When considering absolute infectivity values, addition of TMPRSS2 did increase viral entry in U2OS-ACE2 cells (Fig. S6E). However, the expression of TMPRSS2 was not sufficient to entirely redirect viral entry to a camostat-dependent pathway, in contrast to findings obtained in HEK-ACE2-TMPRSS2 cells. To determine whether U2OS cells may have a lower sensitivity to protease inhibitors, we treated U2OS-ACE2 and U2OS-ACE-TMPRSS2 with different doses of E64D and camostat (Fig. S7A and B), but we did not observe an increase inhibition of PV entry at higher doses. Also, E64D started to induce cell toxicity at the highest dose tested (200  $\mu$ M) (Fig. S7C and D), precluding the testing of even higher doses. The fact that the  $\Delta$ FCS PV entry remained inhibited at 80 to 90% by 50  $\mu$ M E64D in U2OS-ACE2 and U2OS-ACE2-TMPRSS2 cells (Fig. 8D and E) also suggested that the inhibitor was functional in those cells. For the other PV tested, the partial entry inhibition observed with combined camostat-E64D treatment raised the possibility of an additional entry route that would not depend on TMPRSS2 or cathepsins.

## DISCUSSION

This study demonstrates that spikes carrying the S1/S2 cleavage site mutations characteristic of SARS-CoV-2 variants rely on the additional D614G mutation to maintain efficient viral entry. The acquisition of the D614G mutation was already viewed as a key event that enabled the worldwide dissemination of the original SARS-CoV-2 strain (3, 4). We report here that D614G is even more important for the fitness of virions carrying the P681R/H mutations, in particular when the endosomal entry pathway predominates. Indeed, the benefit conferred by D614G on infectivity was 1.5 to 3 times higher for pseudoviruses carrying the P681R/H mutations than for those with the original P681 residue in HEK-ACE2 cells. Based on these findings, we propose that acquisition of D614G played an essential role in the emergence of the highly transmissible and pathogenic Alpha and Delta variants.

We had previously shown that P681H was the key mutation involved in conferring a higher fusogenicity to the Alpha spike (43). We report in the present study that the P681R mutation found in the Delta spike confers an even higher fusogenic capacity, consistent with recent literature (45, 47, 52). In a D614 context, these highly fusogenic spikes were characterized by equivalent or slightly lower expression than the Wuhan spike at the surface of producer cells and by decreased incorporation into pseudotyped virions. This may be due to differences in spike trafficking, as premature intracellular fusion events triggered by the P681H/R spikes could perturb protein maturation pathways. Introduction of the D614G mutation slightly increased the surface expression of the P681H spike, but not that of the P681R spike, and did not restore incorporation of these spikes into virions. Thus, the D614G change must have acted primarily after the virion release stage. The P681H/R spikes incorporated into virions showed a clear increase in the degree of cleavage at the S1/S2 site, as expected (17, 46, 47). Introduction of the D614G mutation into the P681H/R spikes did not significantly change their degree of cleavage, as measured by the S2/S0 ratio. The key difference proved to be in the degree of S1 subunit retention on virions, with an S1/S2 ratio increased by a factor 2 to 3 in the presence of the D614G mutation. Of note, increased S1 retention was also seen when D614G was inserted into the original Wuhan spike, as reported here and in previous studies (17, 24). However, due to the higher cleavage rate achieved by the P681H/R spikes, the proportion of S1 subunits retained in the presence of the D614G was higher, accounting for the preferential effect of the D614G change on highly fusogenic spikes.

The infectivity enhancement conferred by the D614G mutation proved higher in the absence of TMPRSS2 overexpression. This was observed in the HEK-ACE2 as well as the U2OS-ACE2 cellular contexts. In addition, the infectivity enhancement remained moderate in Calu-3 cells, which endogenously express TMPRSS2 and enable viral entry via the surface rather than the endosomal route (37). A likely explanation for these findings is that S1 subunit stability is more critical when using the endosomal rather than the TMPRSS2-



dependent surface entry pathway. This notion is compatible with findings by Laporte and colleagues, who reported that the D614G mutation increased spike stability and promoted the use of the cathepsin L-dependent entry pathway (19). SARS-CoV-2 entry via the endosomal route was shown to take longer than via the surface route and to require endosomal acidification (36, 37). A more stable spike is likely to better withstand a long entry process and/or an acidifying environment. Ultrastructural studies suggest that the release of S1 subunits facilitates the transition of the metastable spike trimer to a postfusion conformation and that these changes may at times happen prematurely, before attachment of S1 to its receptor ACE2 (4). For instance, the presence of postfusion trimers lacking S1 has been documented at the surface of virions by cryo-electron microscopy (53), and it is possible that this phenomenon is further triggered within endosomes. The D614G mutation may limit these premature conformational changes, as this mutation was shown to stabilize the noncovalent association of the S1 and S2 subunits within a spike protomer (24). The stabilizing effect of the D614G mutation may thus be particularly relevant in the case of pre-cleaved spikes with a high propensity for fusion, and in cellular contexts that favor the endosomal entry route. Of note, primary human epithelial cells of the nasal mucosa express high levels of cathepsin-L, in contrast to Calu-3 cells (54). The endosomal entry pathway dependent on cathepsin-L may thus be highly relevant for SARS-CoV-2 propagation *in vivo*.

A spike devoid of the polybasic S1/S2 cleavage site ( $\Delta$ FCS) proved defective in the cell-cell fusion assay. In contrast, pseudotypes carrying this spike were highly infectious in the HEK-ACE2 and U2OS-ACE2 cellular contexts, consistent with previous reports (18, 30, 31, 33). These observations highlight a disconnect between fusogenic capacity measured at the cell surface and infectivity, likely due to differences in the subcellular locations involved. Indeed, the  $\Delta$ FCS spike was highly sensitive to E64D inhibition but only minimally sensitive to camostat and thus mediated entry almost exclusively by the endosomal route. This was further confirmed by the low infectivity of  $\Delta$ FCS pseudotypes in Calu-3 cells, where the surface route predominates, as previously reported (29, 32, 33). The  $\Delta$ FCS spike lacks the PRRA sequence but retains an arginine at 685 and may thus be cleaved at this site (or at neighboring sites) by cathepsins, accounting for its capacity to mediate entry through endosomes. Of note, the presence of the D614G mutation did not restore the fusogenic capacity of the  $\Delta$ FCS spike and induced only limited changes in its infectivity pattern. Indeed, D614G tended to decrease, rather than increase, the infectivity of  $\Delta$ FCS pseudotypes in HEK-ACE2 cells, slightly increased infectivity in U2OS-ACE2 cells, and had no effect on infectivity in Calu-3 cells. These observations further support the notion that D614G acts through stabilization of S1/S2 association, as D614G loses its effects in situations where S1 and S2 are covalently associated.

The sensitivity of pseudotyped viruses to entry inhibitors did not appear dependent on the D614G mutation. Thus, D614G modulated the magnitude of infection but not the proportion of infection that took place through the surface or the endosomal entry routes. Rather, the choice of entry route varied according to the cell line studied, suggesting that it mainly depended on host cell characteristics. As expected (19, 29, 36, 37, 39), the expression of TMPRSS2 redirected most of entry through the surface route in HEK-ACE2-TMPRSS2 as well as Calu-3 cells. The findings in U2OS-ACE2 cells were more intriguing, as neither camostat nor E64D could fully block pseudotyped virus entry in this cell line (with the exception of  $\Delta$ FCS). Further, expression of TMPRSS2 in these cells did not fully redirect viral entry to a camostat-sensitive pathway. These observations raise the possibility of an additional entry pathway that would be insensitive to both camostat and E64D and would thus not depend on TMPRSS2 or on cathepsins. This putative pathway would still require a polybasic S1/S2 cleavage site, as it did not play a role in the entry of the  $\Delta$ FCS pseudotyped virus. One may note that alternate receptors have been recently proposed for SARS-CoV-2 (55), which may provide a basis for alternate entry routes. Additional proteases, such as the metalloproteases ADAM10 and ADAM17 (18, 56, 57) and the coagulation factors Xa and thrombin

(58), have also been proposed to play a role in SARS-CoV-2 entry. A possible role for furin in directly cleaving the S2' site (59), in addition to the S1/S2 site, could also contribute to an alternate entry pathway in U2OS-ACE2 cells.

The T716I mutation found in the Alpha spike had an overall deleterious effect on pseudotyped virus infectivity, which was associated with decreased spike incorporation into virions. In addition, the T716I mutation induced slightly less spike cleavage but markedly lower retention of cleaved S1 subunits. Taken together, the results suggest that the T716I change resulted in a small amount of functional spike carrying the S1 subunit on virions, accounting for a low infectivity. These observations are compatible with structural studies showing that the T716I mutation has a locally destabilizing effect, by abrogating an intraspike protomer hydrogen bond (60). Combination of D614G with the T716I mutation did have a stabilizing effect, as S1 retention improved. However, the infectivity of the D614G/T716I pseudotypes remained lower than that of other mutants in all the cell lines tested. The presence of T716I change may help explain why Alpha pseudotypes retain a low infectivity in HEK-ACE2 cells. On the other hand, Alpha pseudotypes are as infectious as WT-G614 pseudotypes in U2OS-ACE2 and Calu-3 cells, implying that the deleterious effect of T716I is compensated for by other mutations present in the Alpha spike. Reasons for the conservation of a destabilizing mutation such as T716I remain to be fully elucidated, but they may be related to the capacity of the Alpha spike trimer to more frequently switch to an RBD up conformation competent for ACE2 binding (60). Overall, structural studies point to the interplay of several stabilizing and destabilizing mutations that control the degree of exposure of the RBD.

Compensatory mutations that increase entry of the Alpha spike act through several mechanisms. A two-residue deletion found in the N-terminal domain of the Alpha spike,  $\Delta$ H69V70, was reported to increase total spike incorporation into virions (61). In contrast, the D614G change acts primarily through the stabilization of the S1/S2 non-covalent association, as discussed above. The N501Y change found in the RBD increases affinity of the spike for ACE2 by a factor up to 5, which promotes viral entry (26, 60). The P681H mutation increased spike fusogenicity, which should have an impact on viral entry. However, P681H by itself did not increase infectivity in our assays, consistent with a previous report (41). Possible reasons include the instability of the cleaved S1 subunit, which may not be fully compensated for by the D614G change, and a trend toward lower incorporation of the P681H spike into pseudovirions. While the P681H change does not directly increase infectivity of the Alpha variant, at least *in vitro*, it may contribute its pathogenic potential through the facilitation of cell-cell fusion. A pathogenic role for syncytia in pulmonary alveoli has been proposed (52, 62), which may help account for increased pathogenicity of the Alpha variant compared to that of the original Wuhan strain (63). The increased fusogenicity associated with the P681R mutation is even more marked, which may contribute to the superior pathogenicity of the Delta variant (12). The recently emerged variant Omicron expresses a spike with reduced fusogenic capacity (14, 48) and has shown signs of decreased pathogenicity (16), further supporting an association between these two parameters.

Epidemiological and modeling studies have shown that the Alpha VOC had increased transmissibility compared to the D614G SARS-CoV-2 strain (6, 64). In addition, the Delta VOC showed a further increase in transmissibility over the Alpha VOC (11). These findings were not recapitulated in our *in vitro* study, as we did not observe a higher infectivity of the Alpha and Delta pseudoviruses over the D614G reference pseudovirus. Further, the analysis of point mutations showed that the P681H/R changes had a deleterious effect on infectivity that was partially or fully reversed by the D614G change but that did not result in a higher infectivity for the P681H/R-D614G combination. This discrepancy with *in vivo* observations suggests that the pseudovirus system used does not recapitulate all aspects of SARS-CoV-2 infectivity. For instance, it is possible that SARS-CoV-2 can also spread from cell to cell *in vivo*, a phenomenon that cannot be reproduced in single-cycle infectivity assays. This may help explain why increased fusogenicity does not translate into higher infectivity *in vitro*. Another possibility is that highly fusogenic spikes induce a degree of

cytotoxicity when overexpressed in producer cells, which may contribute to a lower spike incorporation into pseudovirions, as observed for the P681R spike.

It remains intriguing that the Omicron variant retains the P681H change in its spike, in spite of its low fusogenic capacity and a reported low degree of S1/S2 cleavage (48). Omicron carries 33 nonsynonymous spike mutations compared to the Wuhan strain, an unprecedented number of changes that induce a remodeling of the N-terminal domain (NTD) and RBD surfaces and result in immune evasion of most classes of monoclonal antibodies (65). These changes also impact the viral entry step, as Omicron infectivity is hampered under conditions of low ACE2 expression (66), a property that may explain the low infectivity of Omicron for lung alveolar tissue (49). Structurally, the regions that control RBD flipping appear more structured in the Omicron trimer, which may slow down the transition of the RBD to the up position and thus make ACE2 binding a rate-limiting step in viral entry (66). Residues close to the FCS also appear more structured, which may limit access of the furin enzyme and account for the low cleavage rate. Thus, low fusogenicity of Omicron appears to result from combinatorial changes that restrict several steps of the entry process but accommodate a wide array of immune escape mutations.

The SARS-CoV-2 virus is demonstrating remarkable adaptability in the face of worldwide vaccination efforts and mounting natural immunity. Due to the plasticity of the spike, emerging variants could adopt distinct evolutionary strategies, based on different degrees of trade-off between transmissibility, pathogenicity, and immune escape. It remains striking, however, that all the SARS-CoV-2 variants relied on the D614G mutation for S1 subunit stabilization. We report that the dependency on the D614G mutation was more marked for highly fusogenic spikes, implying a key role of the D614G mutation in the emergence of highly pathogenic SARS-CoV-2 variants.

## MATERIALS AND METHODS

**Plasmids.** All the spike mutations were inserted into a codon-optimized version of the Wuhan-Hu-1 SARS-CoV-2 spike (GenBank accession no. [QHD43416.1](#)) cloned into a pHCMV backbone (GenBank accession no. [AJ318514](#)). Mutations were introduced into the pHCMV-Spike plasmids using mutagenic primers and the Q5 site-directed mutagenesis kit (New England Biolabs [NEB]). In addition, a truncation of 19 amino acids was introduced into the cytoplasmic tail of each spike studied (deletion at amino acids 1255 to 1273 in the Wuhan-Hu-1 spike) to promote spike incorporation into lentiviral particles, as described previously (67, 68). All the mutant plasmids were sequenced prior to use. Primers used for mutagenesis and sequencing are reported in Table S1. The plasmid pQCXIP-empty was used as a negative control for spike expression (50). Plasmids used to produce GFP-expressing lentiviruses were the lentivector backbone pCDH-EF1 $\alpha$ -GFP (System Biosciences), the packaging plasmid psPAXII (Addgene), and the pRev plasmid (a gift from P. Charneau). For the production of luciferase-expressing lentivirus, the plasmids used were pHAGE-CMV-Luc2-IRES-ZsGreen (NR-52516), pHDM-Hgpm2 (NR-52517), pHDM-tat1b (NR-52518), pRC-CMV-rev1b (NR-52519), all generated in J. Bloom's laboratory (69) and obtained from BEI Resources (kit NR-53816).

**Cell lines.** HEK 293Tn (purchased from SBI Biosciences) and Calu-3 (ATCC HTB55) cells were maintained in Dulbecco's modified Eagle medium (DMEM) and DMEM-F12, respectively, supplemented with 10% fetal bovine serum and 100  $\mu$ g/mL penicillin/streptomycin (DMEMc). Cell lines transduced with ACE2 and/or TMPRSS2 are described elsewhere (50). HEK 293T-hACE2-TMPRSS2 cells (called HEK-ACE2-TMPRSS2 cells here) were induced for TMPRSS2 expression by addition of doxycycline (0.5  $\mu$ g/mL; Sigma) and were maintained in DMEMc with blasticidin (10  $\mu$ g/mL; InvivoGen) and puromycin (1  $\mu$ g/mL; Alfa Aesar). U2OS cells expressing hACE2 and GFP1-10 or hACE2, TMPRSS2, and GFP1-10 were maintained in DMEMc supplemented with blasticidin (10  $\mu$ g/mL; InvivoGen), puromycin (1  $\mu$ g/mL; Alfa Aesar), and hygromycin B (0.2 mg/mL). HEK 293T and Vero-E6 cells expressing GFP1-10 and GFP11 were maintained in DMEMc supplemented with 1  $\mu$ g/mL and 4  $\mu$ g/mL of puromycin, respectively. All the cell lines were cultured at 37°C under a 5% CO<sub>2</sub> atmosphere and were routinely screened for mycoplasma.

**Transfection of HEK 293Tn cells with spike vectors.** Transfection was performed with Lipofectamine 2000 (Thermo Fisher, 11668019), using 125 ng of pHCMV-Spike plasmid diluted in Opti-MEM medium in a final volume of 25  $\mu$ L. DNA was incubated with 0.9  $\mu$ L Lipofectamine 2000 diluted in 25  $\mu$ L Opti-MEM medium, and the mixture was incubated for 20 min before being added to 0.1 million HEK 293Tn cells seeded in a 96-well plate. Transfection efficiency was assessed 18 h posttransfection by monitoring spike surface expression by flow cytometry.

**Production of spike-pseudotyped lentivectors.** GFP lentiviral particles pseudotyped with the SARS-CoV-2 spike were prepared by transfection of HEK 293Tn cells using the CaCl<sub>2</sub> method. The lentiviral vector pCDH-EF1 $\alpha$ -GFP, the packaging plasmid psPAXII, the spike expression vector pHCMV-Spike, and the pRev plasmid were mixed at a 2:2:1:1 ratio, with a total DNA amount of 252  $\mu$ g used per 175-cm<sup>2</sup> flask. The pQCXIP-empty plasmid was used to generate a spike-negative control. At 48 h posttransfection, supernatants were collected and spun for 5 min at 270  $\times$  g for 5 min at 4°C to remove cell

debris. Lentiviral particles were then concentrated by ultracentrifugation at  $23,000 \times g$  for 1.5 h at 4°C onto a 20% sucrose cushion. The viral particle pellet was resuspended in phosphate-buffered saline (PBS) and frozen in aliquots at  $-80^{\circ}\text{C}$  until use.

Luciferase lentiviral particles were produced according to the same protocol but with different plasmid ratios: the lentiviral backbone pHAGE-CMV-Luc2-IRES-ZsGreen, the packaging plasmid pHDM-Hgpm2, the Tat and Rev plasmids pHDM-tat1b and pRC-CMV-rev1b, and the spike plasmid pHCMV-Spike were used at 4.4:1:1:1:1.5 to transfect a 175-cm<sup>2</sup> flask. The pseudotyped lentiviral particles were normalized according to their capsid content, by measuring the Gag p24 antigen concentration with the Alliance HIV-1 p24 antigen enzyme-linked immunosorbent assay (ELISA) kit (Perkin Elmer).

**Infection with spike-pseudotyped lentivectors.** The day before infection with spike-pseudotyped GFP-expressing lentivectors, 100,000 HEK-ACE2-TMPRSS2 cells were plated in 96-well plates, and TMPRSS2 was induced when needed by the addition of doxycycline. HEK-ACE2 cells with and without TMPRSS2 were infected with serial  $2 \times$  dilutions of GFP lentivectors, ranging from 0.0625  $\mu\text{g}$  to 0.5  $\mu\text{g}$  of p24 Gag content in a final volume of 100  $\mu\text{L}$ . Cells were cultivated in the presence of lentivectors, and infection was quantified at 2 days postinfection (p.i.) by measuring the percentage of GFP<sup>+</sup> cells by flow cytometry.

For infection with spike-pseudotyped luciferase lentivectors, the cells were plated in flat-bottom 96-well plates the day before infection in the following numbers: 20,000 U2OS GFP1-10 ACE2 cells with and without TMPRSS2, 50,000 HEK 293T ACE2 cells with and without TMPRSS2, or 50,000 Calu-3 cells. HEK and U2OS cells were infected with 0.125  $\mu\text{g}$  of p24 Gag equivalent, while Calu-3 cells were infected with 1  $\mu\text{g}$  of p24 Gag equivalent, all in a final volume of 100  $\mu\text{L}$ . Two days p.i., medium was removed and replaced with 30  $\mu\text{L}$  DMEM without red phenol. The same volume of luciferase Bright-Glo substrate (Promega) was added before acquisition of luminescence on a Wallac Victor2 1420 multilabel counter (Perkin Elmer system, v3.00.0.53). Infectivity was expressed in relative luciferase units (RLU). For infections experiments in the presence of protease inhibitors, cells were pretreated for 2 h before infection with 100  $\mu\text{M}$  E64-D (Enzo Life Sciences, BML-P1107-0001), 100  $\mu\text{M}$  camostat (CliniSciences, HY-13512), or both, in a final volume of 50  $\mu\text{L}$ . For infection, 50  $\mu\text{L}$  of medium containing 0.065  $\mu\text{g}$  of p24 Gag equivalent was added to HEK ACE2 cells with and without TMPRSS2 and U2OS ACE2 cells with and without TMPRSS2, while 0.5  $\mu\text{g}$  of p24 Gag equivalent in 50  $\mu\text{L}$  was added to Calu-3 cells, resulting in a  $2 \times$  dilution of the protease inhibitors. Infection was monitored at 2 days p.i. by measuring luciferase activity, as described above. The percentage of infectivity inhibition was computed as follows:  $[1 - (\text{RLU treated} / \text{RLU untreated})] \times 100$ .

**Western blotting.** To prepare protein extracts, 2 million cells were lysed in buffer containing 150 mM NaCl, 50 mM Tris HCl (pH 8), 1% Triton, 5 mM EDTA, with  $1 \times$  protease inhibitor cocktail (Roche, 11873580001) for 30 min on ice. For lentiviral particle extracts, an equivalent of 300 ng of Gag p24 was lysed in ELISA lysis buffer containing 1% Triton (Alliance HIV-1 p24 antigen ELISA kit; Perkin Elmer) and protease inhibitors for 30 min on ice. Samples were heated and reduced in  $1 \times$  final dithiothreitol (DTT) buffer (Thermo Fisher, NP0004) at  $90^{\circ}\text{C}$  for 10 min before being run on a 4-to-12% acrylamide denaturing gel (Thermo Fisher, NP0323 NuPAGE). Proteins were then transferred onto a nitrocellulose membrane (Thermo Fisher, IB23001). The membrane was blocked with 5% dried milk in 0.1% PBS-Tween, before incubation with three primary antibodies (S1, S2, and p24 Gag or actin) for 1 h at room temperature (RT), followed by 3 washes in 0.1% PBS-Tween and incubation with secondary antibodies for 30 min at RT. After 3 more washes, the fluorescent signal was revealed on a Li-Cor Odyssey CLx 9140 imaging system. Images were quantified with the Image Studio Lite (v5.2.5) software, using a mode with automated background subtraction. Primary antibodies consisted of two antispike antibodies (rabbit anti-S1 [GeneTex, GTX135356], 1:1,000; mouse anti-S2 [GeneTex, GTX632604], 1:1,000), and one normalization antibody, mouse anti-p24 Gag (R&D Systems, MAB7360; 1:1,000) or mouse antiactin (Cell Signaling, 8H10D10; 1:2,000). Anti-rabbit and anti-mouse IgG secondary antibodies, conjugated to DyLight-800 (Bethyl Laboratories, A80-304D8) and DyLight-680 (Thermo Fisher, SA5-35521), respectively, were each used at a 1:5,000 dilution.

**Cell-cell fusion assay.** For the cell-cell fusion assay, 15,000 GFP1-10-expressing HEK 293T were transfected with pHCMV-Spike vectors, washed with DMEM supplemented with 10% fetal calf serum without antibiotics (DMEMna), and then mixed at a 1:1 ratio with GFP11-expressing Vero-E6 cells. Briefly, 10 ng of spike plasmid and 90 ng of empty vector were mixed in 25  $\mu\text{L}$  Opti-MEM medium. Then, 0.3  $\mu\text{L}$  Lipofectamine 2000 diluted in 25  $\mu\text{L}$  Opti-MEM medium was added to the DNA, and the mixture was incubated for 30 min before being added to HEK GFP1-10 cells. After 30 min, transfected cells were washed in DMEMna and spun at  $500 \times g$  for 5 min before being mixed at a 1:1 ratio with Vero GFP11 cells in DMEMna. Cells were stained with Hoechst. Cells were cultivated for 18 h in transparent-bottom plates ( $\mu\text{Clear}$ , 655090). Fusion measurement was assessed on an Opera Phenix high-content screening system (PerkinElmer), by automatically measuring the GFP area normalized to the total number of nuclei.

**Flow cytometry.** To quantify cells infected by GFP lentivectors, cells were harvested, washed in PBS, and stained with the viability dye Aqua (Invitrogen) at a 1:800 dilution in PBS for 30 min at 4°C. After two washes in PBS, cells were fixed with 2% paraformaldehyde (PFA) (Thermo Fisher, 43368-9M) and acquired on an Attune NxT flow cytometer. To quantify spike expression in transfected HEK 293Tn cells, cells were harvested as described above and stained with the pan-SARS-CoV-2 S1 human MAb 129 or the pan-SARS-CoV-2 S2 human MAb 10 (43) at 1  $\mu\text{g}/\text{mL}$  for 30 min at 4°C. Alternatively, cells were stained with the murine anti-S2 MAb GTX-S2 (GeneTex, GTX632604) at 10  $\mu\text{g}/\text{mL}$ . After two PBS washes, cells were stained with the viability dye Aqua (1:800) and a goat anti-human IgG-AF647 antibody (Thermo Fisher, A21445) or a goat anti-mouse IgG-AF647 antibody (Invitrogen, 2161043) at 1:500 for

30 min at 4°C. Samples were fixed with 2% PFA before acquisition on the NxT flow cytometer. Data were analyzed with the FlowJo software v10.8.1 (Becton Dickinson).

To evaluate ACE2 and TMPRSS2 expression in the target cell lines used, cells were surface labeled with the goat anti-ACE2 antibody (R&D, AF933) at 5 mg/mL for 30 min at 4°C. After being washed, cells were incubated with the secondary antibody donkey anti-goat-AF647 (Thermo Fisher, A21447) at a 1:500 dilution. Cells were then permeabilized with the Fix/Perm kit (BD Biosciences, 554714) according to manufacturer recommendations. Cells were intracellularly stained with a rabbit anti-TMPRSS2 antibody (Atlas Antibodies, HPA035787) at 0.3 mg/mL. After a washing, the secondary staining was done with a donkey anti-rabbit-AF555 antibody (Fisher, 16229260) at a 1:500 dilution. Cells were then fixed in 2% PFA and analyzed by flow cytometry as described above.

**Statistical analysis.** All statistical analyses were carried out with the GraphPad Prism software (v9). The tests used and significance thresholds are stated in the figure legends. Mutants with mutations in the D614 backbone were compared to the WT D614 spike, while mutants with mutations in the G614 backbone were compared to the WT G614 spike. Statistics were computed for all spikes studied by one-way analysis of variance (ANOVA) with a Holm-Šidák correction for multiple comparisons. For G614/D614 ratio analyses, we evaluated by one-sample *t* test whether each ratio significantly differed from 1. All the graphs were generated in GraphPad Prism, except for the spider plots, which were made using Microsoft Excel (v16.16.27).

## SUPPLEMENTAL MATERIAL

Supplemental material is available online only.

**SUPPLEMENTAL FILE 1**, PDF file, 6.1 MB.

## ACKNOWLEDGMENTS

We thank Nathalie Aulner and the UTechS Photonic BiImaging (UPBI) core facility of Institut Pasteur, a member of the France BiImaging network, for training on the Opera imaging system. We thank Jacob Seeler for help with gel image acquisition and all the members of the Virus and Immunity Unit for reagents and helpful discussions. The following reagent was obtained through BEI Resources, NIAID, NIH: SARS-related coronavirus 2, Wuhan-Hu-1 spike-pseudotyped lentiviral kit V2, NR-53816.

This work was supported by the Urgence COVID-19 Fundraising Campaign of Institut Pasteur (COROCHIP, PFR4, and PFR7 projects) and Agence Nationale de Recherche sur le SIDA et les Maladies Infectieuses Emergentes (ANRS-MIE; project 19206) (L.A.C.) and by the Pasteur Institute, the European Health Emergency Preparedness and Response Authority (HERA), Urgence COVID-19 Fundraising Campaign of Institut Pasteur, Fondation pour la Recherche Médicale (FRM), ANRS-MIE, the Vaccine Research Institute (ANR-10-LABX-77), Labex IBEID (ANR-10-LABX-62-IBEID), ANR/FRM Flash Covid PROTEO-SARS-CoV-2, ANR Coronamito, and IDISCOVER (O.S.). S.G. is the recipient of an MESR/Ecole Doctorale BioSPC, Université Paris Cité, fellowship; R.R. is the recipient of a Sidaction fellowship; and J.K. is the recipient of an ANRS fellowship.

Conceptualization: Stacy Gellenoncourt, Olivier Schwartz, Lisa A. Chakrabarti; Funding acquisition: Olivier Schwartz, Lisa A. Chakrabarti; Investigation: Stacy Gellenoncourt, Nell Saunders, Rémy Robinot, Lucas Auguste, Maaran Michael Rajah, Jérôme Kervevan, Raphaël Jeger-Madiot, Isabelle Staropoli; Methodology: Julian Buchrieser; Resources: Cyril Planchais, Hugo Mouquet; Supervision: Olivier Schwartz, Lisa A. Chakrabarti; Visualization: Stacy Gellenoncourt, Lisa A. Chakrabarti; Writing - Original draft preparation: Stacy Gellenoncourt, Lisa A. Chakrabarti; Writing - Review & editing: Stacy Gellenoncourt, Nell Saunders, Rémy Robinot, Lucas Auguste, Maaran Michael Rajah, Jérôme Kervevan, Raphaël Jeger-Madiot, Isabelle Staropoli, Cyril Planchais, Hugo Mouquet, Julian Buchrieser, Olivier Schwartz, Lisa A. Chakrabarti.

## REFERENCES

1. Tao K, Tzou PL, Nouhin J, Gupta RK, de Oliveira T, Kosakovsky Pond SL, Fera D, Shafer RW. 2021. The biological and clinical significance of emerging SARS-CoV-2 variants. *Nat Rev Genet* 22:757–773. <https://doi.org/10.1038/s41576-021-00408-x>.
2. Minskaia E, Hertzog T, Gorbalenya AE, Campanacci V, Cambillau C, Canard B, Ziebuhr J. 2006. Discovery of an RNA virus 3'→5' exoribonuclease that is critically involved in coronavirus RNA synthesis. *Proc Natl Acad Sci U S A* 103:5108–5113. <https://doi.org/10.1073/pnas.0508200103>.
3. Korber B, Fischer WM, Gnanakaran S, Yoon H, Theiler J, Abfalterer W, Hengartner N, Giorgi EE, Bhattacharya T, Foley B, Hastie KM, Parker MD, Partridge DG, Evans CM, Freeman TM, de Silva TI, McDanal C, Perez LG, Tang H, Moon-Walker A, Whelan SP, LaBranche CC, Saphire EO, Montefiori DC, Angyal A, Brown RL, Carrilero L, Green LR, Groves DC, Johnson KJ, Keeley AJ, Lindsey BB, Parsons PJ, Raza M, Rowland-Jones S, Smith N, Tucker RM, Wang D, Wyles MD. 2020. Tracking changes in SARS-CoV-2

- spike: evidence that D614G increases infectivity of the COVID-19 virus. *Cell* 182:812–827.E19. <https://doi.org/10.1016/j.cell.2020.06.043>.
4. Jackson CB, Farzan M, Chen B, Choe H. 2022. Mechanisms of SARS-CoV-2 entry into cells. *Nat Rev Mol Cell Biol* 23:3–20. <https://doi.org/10.1038/s41580-021-00418-x>.
  5. WHO. 2022. Tracking SARS-CoV-2 variants. <https://www.who.int/en/activities/tracking-SARS-CoV-2-variants/>.
  6. Davies NG, Abbott S, Barnard RC, Jarvis CI, Kucharski AJ, Munday JD, Pearson CAB, Russell TW, Tully DC, Washburne AD, Wenseleers T, Gimma A, Waites W, Wong KLM, van Zandvoort K, Silverman JD, Group CC-W, Consortium C-GU, Diaz-Ordaz K, Keogh R, Eggo RM, Funk S, Jit M, Atkins KE, Edmunds WJ, CMMID COVID-19 Working Group. 2021. Estimated transmissibility and impact of SARS-CoV-2 lineage B.1.1.7 in England. *Science* 372:eabg3055. <https://doi.org/10.1126/science.abg3055>.
  7. Thorne LG, Bouhaddou M, Reuschl AK, Zuliani-Alvarez L, Polacco B, Pelin A, Batra J, Whelan MVX, Hosmillo M, Fossati A, Ragazzini R, Jungreis I, Ummadi M, Rojc A, Turner J, Bischof ML, Obernier K, Braberg H, Soucheray M, Richards A, Chen KH, Harjai B, Memon D, Hiatt J, Rosales R, McGovern BL, Jahun A, Fabius JM, White K, Goodfellow IG, Takeuchi Y, Bonfanti P, Shokat K, Jura N, Verba K, Noursadeghi M, Beltrao P, Kellis M, Swaney DL, Garcia-Sastre A, Jolly C, Towers GJ, Krogan NJ. 2022. Evolution of enhanced innate immune evasion by SARS-CoV-2. *Nature* 602:487–495. <https://doi.org/10.1038/s41586-021-04352-y>.
  8. Ulrich L, Halwe NJ, Taddeo A, Ebert N, Schon J, Devisme C, Truebs BS, Hoffmann B, Wider M, Fan X, Bekliz M, Essaidi-Laziosi M, Schmidt ML, Niemeyer D, Corman VM, Kraft A, Godel A, Laloli L, Kelly JN, Calderon BM, Breithaupt A, Wylezich C, Berenguer Veiga I, Gultom M, Osman S, Zhou B, Adea K, Meyer B, Eberhardt CS, Thomann L, Gsell M, Labrousseau F, Jores J, Summerfeld A, Drosten C, Eckerle IA, Wentworth DE, Dijkman R, Hoffmann D, Thiel V, Beer M, Benarafa C. 2022. Enhanced fitness of SARS-CoV-2 variant of concern Alpha but not Beta. *Nature* 602:307–313. <https://doi.org/10.1038/s41586-021-04342-0>.
  9. Liu L, Iketani S, Guo Y, Chan JF, Wang M, Liu L, Luo Y, Chu H, Huang Y, Nair MS, Yu J, Chik KK, Yuen TT, Yoon C, To KK, Chen H, Yin MT, Sobieszczyk ME, Huang Y, Wang HH, Sheng Z, Yuen KY, Ho DD. 2022. Striking antibody evasion manifested by the omicron variant of SARS-CoV-2. *Nature* 602:676–681. <https://doi.org/10.1038/s41586-021-04388-0>.
  10. Planas D, Bruel T, Grzelak L, Guivel-Benhassine F, Staropoli I, Porrot F, Planchais C, Buchrieser J, Rajah MM, Bishop E, Albert M, Donati F, Prot M, Behillil S, Enouf V, Maquart M, Smati-Lafarge M, Varon E, Schortgen F, Yahyaoui L, Gonzalez M, De Seze J, Pere H, Veyer D, Seve A, Simon-Loriere E, Fafi-Kremer S, Stefic K, Mouquet H, Hocqueloux L, van der Werf S, Prazuck T, Schwartz O. 2021. Sensitivity of infectious SARS-CoV-2 B.1.1.7 and B.1.351 variants to neutralizing antibodies. *Nat Med* 27:917–924. <https://doi.org/10.1038/s41586-021-01318-5>.
  11. Mlcochova P, Kemp SA, Dhar MS, Papa G, Meng B, Ferreira IATM, Datir R, Collier DA, Albecka A, Singh S, Pandey R, Brown J, Zhou J, Goonawardane N, Mishra S, Whittaker C, Mellan T, Marwal R, Datta M, Sengupta S, Ponnusamy K, Radhakrishnan VS, Abdullahi A, Charles O, Chattopadhyay P, Devi P, Caputo D, Peacock T, Wattal C, Goel N, Satwik A, Vaishya R, Agarwal M, Chauhan H, Dikid T, Gogia H, Lall H, Verma K, Dhar MS, Singh MK, Soni N, Meena N, Madan P, Singh P, Sharma R, Sharma R, Kabra S, Kumar S, Kumari S, Sharma U, The Indian SARS-CoV-2 Genomics Consortium (INSACOG), et al. 2021. SARS-CoV-2 B.1.617.2 Delta variant replication and immune evasion. *Nature* 599:114–119. <https://doi.org/10.1038/s41586-021-03944-y>.
  12. Twohig KA, Nyberg T, Zaidi A, Thelwall S, Sinnathamby MA, Aliabadi S, Seaman SR, Harris RJ, Hope R, Lopez-Bernal J, Gallagher E, Charlett A, De Angelis D, Presanis AM, Dabrera G, COVID-19 Genomics UK (COG-UK) consortium. 2022. Hospital admission and emergency care attendance risk for SARS-CoV-2 delta (B.1.617.2) compared with alpha (B.1.1.7) variants of concern: a cohort study. *Lancet Infect Dis* 22:35–42. [https://doi.org/10.1016/S1473-3099\(21\)00475-8](https://doi.org/10.1016/S1473-3099(21)00475-8).
  13. Viana R, Moyo S, Amoako DG, Tegally H, Scheepers C, Althaus CL, Anyaneji UJ, Bester PA, Boni MF, Chand M, Choga WT, Colquhoun R, Davids M, Deforche K, Doolabh D, du Plessis L, Engelbrecht S, Everatt J, Giandhari J, Giovanetti M, Hardie D, Hill V, Hsiao NY, Iranzadeh A, Ismail A, Joseph C, Joseph R, Koopile L, Kosakovsky Pond SL, Kraemer MUG, Kuate-Lere L, Laguda-Akingba O, Lesetedi-Mafoko O, Lessells RJ, Lockman S, Lucaci AG, Maharaj A, Mahlungu B, Mponga T, Mahlakwane K, Makatini Z, Marais G, Maruapula D, Masupu K, Matshaba M, Mayaphi S, Mbhele N, Mbulawa MB, Mendes A, Mlisana K, et al. 2022. Rapid epidemic expansion of the SARS-CoV-2 Omicron variant in southern Africa. *Nature* 603:679–686. <https://doi.org/10.1038/d41586-021-03832-5>.
  14. Suzuki R, Yamasoba D, Kimura I, Wang L, Kishimoto M, Ito J, Morioka Y, Nao N, Nasser H, Uriu K, Kosugi Y, Tsuda M, Orba Y, Sasaki M, Shimizu R, Kawabata R, Yoshimatsu K, Asakura H, Nagashima M, Sadamasu K, Yoshimura K, Suganami M, Oide A, Chiba M, Ito H, Tamura T, Tsushima K, Kubo H, Ferdous Z, Mouri H, Iida M, Kasahara K, Tabata K, Ishizuka M, Shigeno A, Tokunaga K, Ozono S, Yoshida I, Nakagawa S, Wu J, Takahashi M, Kaneda A, Seki M, Fujiki R, Nawai BR, Suzuki Y, Kashima Y, Abe K, Imamura K, Shirakawa K, The Genotype to Phenotype Japan (G2P-Japan) Consortium, et al. 2022. Attenuated fusogenicity and pathogenicity of SARS-CoV-2 Omicron variant. *Nature* 603:700–705. <https://doi.org/10.1038/s41586-022-04462-1>.
  15. Planas D, Saunders N, Maes P, Guivel-Benhassine F, Planchais C, Buchrieser J, Bolland WH, Porrot F, Staropoli I, Lemoine F, Pere H, Veyer D, Puech J, Rodary J, Baele G, Dellicour S, Raymenants J, Gorissen S, Geenen C, Vanmechelen B, Wawina-Bokalanga T, Marti-Carreras J, Cuyppers L, Seve A, Hocqueloux L, Prazuck T, Rey F, Simon-Loriere E, Bruel T, Mouquet H, Andre E, Schwartz O. 2021. Considerable escape of SARS-CoV-2 Omicron to antibody neutralization. *Nature* 602:671–675. <https://doi.org/10.1038/s41586-021-04389-z>.
  16. Wolter N, Jassat W, Walaza S, Welch R, Moultrie H, Groome M, Amoako DG, Everatt J, Bhiman JN, Scheepers C, Tebeila N, Chiwandire N, du Plessis M, Govender N, Ismail A, Glass A, Mlisana K, Stevens W, Treurnicht FK, Makatini Z, Hsiao NY, Parboosing R, Wadula J, Hussey H, Davies MA, Boule A, von Gottberg A, Cohen C. 2022. Early assessment of the clinical severity of the SARS-CoV-2 omicron variant in South Africa: a data linkage study. *Lancet* 399:437–446. [https://doi.org/10.1016/S0140-6736\(22\)00017-4](https://doi.org/10.1016/S0140-6736(22)00017-4).
  17. Zhang L, Jackson CB, Mou H, Ojha A, Peng H, Quinlan BD, Rangarajan ES, Pan A, Vanderheiden A, Suthar MS, Li W, Izard T, Rader C, Farzan M, Choe H. 2020. SARS-CoV-2 spike-protein D614G mutation increases virion spike density and infectivity. *Nat Commun* 11:6013. <https://doi.org/10.1038/s41467-020-19808-4>.
  18. Nguyen HT, Zhang S, Wang Q, Anang S, Wang J, Ding H, Kappes JC, Sodroski J. 2020. Spike glycoprotein and host cell determinants of SARS-CoV-2 entry and cytopathic effects. *J Virol* 95:e02304-20. <https://doi.org/10.1128/JVI.02304-20>.
  19. Laporte M, Raeymaekers V, Van Berwaer R, Vandepuit J, Marchand-Casas I, Thibaut HJ, Van Looveren D, Martens K, Hoffmann M, Maes P, Pohlmann S, Naesens L, Stevaert A. 2021. The SARS-CoV-2 and other human coronavirus spike proteins are fine-tuned towards temperature and proteases of the human airways. *PLoS Pathog* 17:e1009500. <https://doi.org/10.1371/journal.ppat.1009500>.
  20. Plante JA, Liu Y, Liu J, Xia H, Johnson BA, Lokugamage KG, Zhang X, Muruato AE, Zou J, Fontes-Garfias CR, Mirchandani D, Scharton D, Billello JP, Ku Z, An Z, Kalveram B, Freiberg AN, Menachery VD, Xie X, Plante KS, Weaver SC, Shi P-Y. 2021. Spike mutation D614G alters SARS-CoV-2 fitness. *Nature* 592:116–121. <https://doi.org/10.1038/s41586-020-2895-3>.
  21. Zhou B, Thao TTN, Hoffmann D, Taddeo A, Ebert N, Labrousseau F, Pohlmann A, King J, Steiner S, Kelly JN, Portmann J, Halwe NJ, Ulrich L, Truebs BS, Fan X, Hoffmann B, Wang L, Thomann L, Lin X, Stalder H, Pozzi B, de Brot S, Jiang N, Cui D, Hossain J, Wilson MM, Keller MW, Stark TJ, Barnes JR, Dijkman R, Jores J, Benarafa C, Wentworth DE, Thiel V, Beer M. 2021. SARS-CoV-2 spike D614G change enhances replication and transmission. *Nature* 592:122–127. <https://doi.org/10.1038/s41586-021-03361-1>.
  22. Yurkovetskiy L, Wang X, Pascal KE, Tomkins-Tinch C, Nyalile TP, Wang Y, Baum A, Diehl WE, Dauphin A, Carbone C, Veinotte K, Egri SB, Schaffner SF, Lemieux JE, Munro JB, Rafique A, Barve A, Sabeti PC, Kyrtasous CA, Dudkina NV, Shen K, Luban J. 2020. Structural and functional analysis of the D614G SARS-CoV-2 spike protein variant. *Cell* 183:739–751.E8. <https://doi.org/10.1016/j.cell.2020.09.032>.
  23. Benton DJ, Wrobel AG, Roustan C, Borg A, Xu P, Martin SR, Rosenthal PB, Skehel JJ, Gamblin SJ. 2021. The effect of the D614G substitution on the structure of the spike glycoprotein of SARS-CoV-2. *Proc Natl Acad Sci U S A* 118:e2022586118. <https://doi.org/10.1073/pnas.2022586118>.
  24. Zhang J, Cai Y, Xiao T, Lu J, Peng H, Sterling SM, Walsh RM, Jr, Rits-Volloch S, Zhu H, Woosley AN, Yang W, Sliz P, Chen B. 2021. Structural impact on SARS-CoV-2 spike protein by D614G substitution. *Science* 372:525–530. <https://doi.org/10.1126/science.abf2303>.
  25. Juraszek J, Rutten L, Blokland S, Bouchier P, Voorzaat R, Ritschel T, Bakkers MJG, Renault LLR, Langedijk JPM. 2021. Stabilizing the closed SARS-CoV-2 spike trimer. *Nat Commun* 12:244. <https://doi.org/10.1038/s41467-020-20321-x>.
  26. Liu Y, Liu J, Plante KS, Plante JA, Xie X, Zhang X, Ku Z, An Z, Scharton D, Schindewolf C, Widen SG, Menachery VD, Shi PY, Weaver SC. 2022. The N501Y spike substitution enhances SARS-CoV-2 infection and transmission. *Nature* 602:294–299. <https://doi.org/10.1038/s41586-021-04245-0>.

27. Coutard B, Valle C, de Lamballerie X, Canard B, Seidah NG, Decroly E. 2020. The spike glycoprotein of the new coronavirus 2019-nCoV contains a furin-like cleavage site absent in CoV of the same clade. *Antiviral Res* 176:104742. <https://doi.org/10.1016/j.antiviral.2020.104742>.
28. Walls AC, Park YJ, Tortorici MA, Wall A, McGuire AT, Veesler D. 2020. Structure, function, and antigenicity of the SARS-CoV-2 Spike Glycoprotein. *Cell* 183:1735. <https://doi.org/10.1016/j.cell.2020.11.032>.
29. Shang J, Wan Y, Luo C, Ye G, Geng Q, Auerbach A, Li F. 2020. Cell entry mechanisms of SARS-CoV-2. *Proc Natl Acad Sci U S A* 117:11727–11734. <https://doi.org/10.1073/pnas.2003138117>.
30. Papa G, Mallery DL, Albecka A, Welch LG, Cattin-Ortola J, Luptak J, Paul D, McMahon HT, Goodfellow IG, Carter A, Munro S, James LC. 2021. Furin cleavage of SARS-CoV-2 Spike promotes but is not essential for infection and cell-cell fusion. *PLoS Pathog* 17:e1009246. <https://doi.org/10.1371/journal.ppat.1009246>.
31. Lavie M, Dubuisson J, Belouzard S. 2022. SARS-CoV-2 spike furin cleavage site and S2' basic residues modulate the entry process in a host cell-dependent manner. *J Virol* 96:e0047422. <https://doi.org/10.1128/jvi.00474-22>.
32. Hoffmann M, Kleine-Weber H, Pohlmann S. 2020. A multibasic cleavage site in the spike protein of SARS-CoV-2 is essential for infection of human lung cells. *Mol Cell* 78:779–784.E5. <https://doi.org/10.1016/j.molcel.2020.04.022>.
33. Peacock TP, Goldhill DH, Zhou J, Baillon L, Frise R, Swann OC, Kugathasan R, Penn R, Brown JC, Sanchez-David RY, Braga L, Williamson MK, Hassard JA, Staller E, Hanley B, Osborn M, Giacca M, Davidson AD, Matthews DA, Barclay WS. 2021. The furin cleavage site in the SARS-CoV-2 spike protein is required for transmission in ferrets. *Nat Microbiol* 6:899–909. <https://doi.org/10.1038/s41564-021-00908-w>.
34. Johnson BA, Xie X, Bailey AL, Kalveram B, Lokugamage KG, Muruato A, Zou J, Zhang X, Juelich T, Smith JK, Zhang L, Bopp N, Schindewolf C, Vu M, Vanderheiden A, Winkler ES, Swetnam D, Plante JA, Aguilar P, Plante KS, Popov V, Lee B, Weaver SC, Suthar MS, Routh AL, Ren P, Ku Z, An Z, Debbink K, Diamond MS, Shi PY, Freiberg AN, Menachery VD. 2021. Loss of furin cleavage site attenuates SARS-CoV-2 pathogenesis. *Nature* 591:293–299. <https://doi.org/10.1038/s41586-021-03237-4>.
35. Benton DJ, Wrobel AG, Xu P, Roustan C, Martin SR, Rosenthal PB, Skehel JJ, Gamblin SJ. 2020. Receptor binding and priming of the spike protein of SARS-CoV-2 for membrane fusion. *Nature* 588:327–330. <https://doi.org/10.1038/s41586-020-2772-0>.
36. Hoffmann M, Kleine-Weber H, Schroeder S, Kruger N, Herrler T, Erichsen S, Schiergens TS, Herrler G, Wu NH, Nitsche A, Muller MA, Drosten C, Pohlmann S. 2020. SARS-CoV-2 Cell entry depends on ACE2 and TMPRSS2 and is blocked by a clinically proven protease inhibitor. *Cell* 181:271–280.E8. <https://doi.org/10.1016/j.cell.2020.02.052>.
37. Koch J, Uckelely ZM, Doldan P, Stanifer M, Boulant S, Lozach PY. 2021. TMPRSS2 expression dictates the entry route used by SARS-CoV-2 to infect host cells. *EMBO J* 40:e107821. <https://doi.org/10.15252/embj.2021107821>.
38. Laporte M, Stevaert A, Raeymaekers V, Van Berwaer R, Martens K, Pöhlmann S, Naesens L. 2020. The SARS-CoV-2 and other human coronavirus spike proteins are fine-tuned towards temperature and proteases of the human airways. *bioRxiv*. <https://doi.org/10.1101/2020.11.09.374603>.
39. Bestle D, Heindl MR, Limburg H, Van Lam van T, Pilgram O, Moulton H, Stein DA, Harges K, Eickmann M, Dolnik O, Rohde C, Klenk H-D, Garten W, Steinmetzer T, Böttcher-Friebertshäuser E. 2020. TMPRSS2 and furin are both essential for proteolytic activation of SARS-CoV-2 in human airway cells. *Life Sci Alliance* 3:e202000786. <https://doi.org/10.26508/lsa.202000786>.
40. Tian S, Huang Q, Fang Y, Wu J. 2011. FurinDB: a database of 20-residue furin cleavage site motifs, substrates and their associated drugs. *Int J Mol Sci* 12:1060–1065. <https://doi.org/10.3390/ijms12021060>.
41. Brown JC, Goldhill DH, Zhou J, Peacock TP, Frise R, Goonawardane N, Baillon L, Kugathasan R, Pinto AL, McKay PF, Hassard J, Moshe M, Singanayagam A, Burgoyne T, Barclay WS, the ATACCC Investigators, PHE Virology Consortium. 2021. Increased transmission of SARS-CoV-2 lineage B.1.1.7 (VOC 2020212/01) is not accounted for by a replicative advantage in primary airway cells or antibody escape. *bioRxiv*. <https://doi.org/10.1101/2021.02.24.432576>.
42. Escalera A, Gonzalez-Reiche AS, Aslam S, Mena I, Laporte M, Pearl RL, Fossati A, Rathnasinghe R, Alshammari H, van de Guchte A, Farrugia K, Qin Y, Bouhaddou M, Kehrter T, Zuliani-Alvarez L, Meekins DA, Balaraman V, McDowell C, Richt JA, Bajic G, Sordillo EM, Dejosez M, Zwaka TP, Krogan NJ, Simon V, Albrecht RA, van Bakel H, Garcia-Sastre A, Aydiello T. 2022. Mutations in SARS-CoV-2 variants of concern link to increased spike cleavage and virus transmission. *Cell Host Microbe* 30:373–387.E7. <https://doi.org/10.1016/j.chom.2022.01.006>.
43. Rajah MM, Hubert M, Bishop E, Saunders N, Robinot R, Grzelak L, Planas D, Dufloo J, Gellenoncourt S, Bongers A, Zivaljic M, Planchais C, Guivel-Benhassine F, Porrot F, Mouquet H, Chakrabarti LA, Buchrieser J, Schwartz O. 2021. SARS-CoV-2 Alpha, Beta, and Delta variants display enhanced Spike-mediated syncytia formation. *EMBO J* 40:e108944. <https://doi.org/10.15252/embj.2021108944>.
44. Lubinski B, Fernandes MHV, Frazier L, Tang T, Daniel S, Diel DG, Jaimes JA, Whittaker GR. 2022. Functional evaluation of the P681H mutation on the proteolytic activation of the SARS-CoV-2 variant B.1.1.7 (Alpha) spike. *iScience* 25:103589. <https://doi.org/10.1016/j.isci.2021.103589>.
45. Liu Y, Liu J, Johnson BA, Xia H, Ku Z, Schindewolf C, Widen SG, An Z, Weaver SC, Menachery VD, Xie X, Shi P-Y. 2021. Delta spike P681R mutation enhances SARS-CoV-2 fitness over Alpha variant. *bioRxiv*. <https://doi.org/10.1101/2021.08.12.456173>.
46. Peacock TP, Sheppard CM, Brown JC, Goonawardane N, Zhou J, Whiteley M, de Silva TI, Barclay WS. 2021. The SARS-CoV-2 variants associated with infections in India, B.1.617, show enhanced spike cleavage by furin. *bioRxiv*. <https://doi.org/10.1101/2021.05.28.446163>.
47. Saito A, Irie T, Suzuki R, Maemura T, Nasser H, Uriu K, Kosugi Y, Shirakawa K, Sadamasu K, Kimura I, Ito J, Iwatsuki-Horimoto K, Ito M, Yamayoshi S, Loeber S, Tsuda M, Wang L, Ozono S, Butlertanaka EP, Tanaka YL, Shimizu R, Shimizu K, Yoshimatsu K, Kawabata R, Sakaguchi T, Tokunaga K, Yoshida I, Asakura H, Nagashima M, Kazuma Y, Nomura R, Horisawa Y, Yoshimura K, Takaori-Kondo A, Imai M, Tanaka S, Nakagawa S, Ikeda T, Fukuhara T, Kawaoka Y, Sato K, Genotype to Phenotype Japan Consortium. 2022. Enhanced fusogenicity and pathogenicity of SARS-CoV-2 Delta P681R mutation. *Nature* 602:300–306. <https://doi.org/10.1038/s41586-021-04266-9>.
48. Meng B, Abdullahi A, Ferreira IATM, Goonawardane N, Saito A, Kimura I, Yamasoba D, Gerber PP, Fathi S, Rathore S, Zepeda SK, Papa G, Kemp SA, Ikeda T, Toyoda M, Tan TS, Kuramochi J, Mitsunaga S, Ueno T, Shirakawa K, Takaori-Kondo A, Brevini T, Mallery DL, Charles OJ, Baker S, Dougan G, Hess C, Kingston N, Lehner PJ, Lyons PA, Matheson NJ, Ouweland WH, Saunders C, Summers C, Thaventhiran JED, Toshner M, Weekes MP, Maxwell P, Shaw A, Bucke A, Calder J, Canna L, Domingo J, Elmer A, Fuller S, Harris J, Hewitt S, Kennet J, Jose S, Kourampa J, The CITIID-NIHR BioResource COVID-19 Collaboration, et al. 2022. Altered TMPRSS2 usage by SARS-CoV-2 Omicron impacts tropism and fusogenicity. *Nature* 603:706–714. <https://doi.org/10.1038/s41586-022-04474-x>.
49. Hui KPY, Ho JCW, Cheung MC, Ng KC, Ching RHH, Lai KL, Kam TT, Gu H, Sit KY, Hsin MKY, Au TWK, Poon LLM, Peiris M, Nicholls JM, Chan MCW. 2022. SARS-CoV-2 Omicron variant replication in human bronchus and lung ex vivo. *Nature* 603:715–720. <https://doi.org/10.1038/s41586-022-04479-6>.
50. Buchrieser J, Dufloo J, Hubert M, Monel B, Planas D, Rajah MM, Planchais C, Porrot F, Guivel-Benhassine F, Van der Werf S, Casartelli N, Mouquet H, Bruel T, Schwartz O. 2021. Syncytia formation by SARS-CoV-2-infected cells. *EMBO J* 40:e107405. <https://doi.org/10.15252/embj.202107405>.
51. Buchrieser J, Degrelle SA, Couderc T, Nevers Q, Disson O, Manet C, Donahue DA, Porrot F, Hillion KH, Perthame E, Arroyo MV, Souquere S, Ruigrok K, Dupressoir A, Heidmann T, Montagutelli X, Fournier T, Lecuit M, Schwartz O. 2019. IFITM proteins inhibit placental syncytiotrophoblast formation and promote fetal demise. *Science* 365:176–180. <https://doi.org/10.1126/science.aaw7733>.
52. Rajah MM, Bernier A, Buchrieser J, Schwartz O. 2021. The mechanism and consequences of SARS-CoV-2 spike-mediated fusion and syncytia formation. *J Mol Biol* 434:167280. <https://doi.org/10.1016/j.jmb.2021.167280>.
53. Klein S, Cortese M, Winter SL, Wachsmuth-Melm M, Neufeldt CJ, Cerikan B, Stanifer ML, Boulant S, Bartenschlager R, Chlanda P. 2020. SARS-CoV-2 structure and replication characterized by in situ cryo-electron tomography. *Nat Commun* 11:5885. <https://doi.org/10.1038/s41467-020-19619-7>.
54. Willett BJ, Grove J, MacLean OA, Wilkie C, De Lorenzo G, Furnon W, Cantoni D, Scott S, Logan N, Ashraf S, Manali M, Szemiel A, Cowton V, Vink E, Harvey WT, Davis C, Asamaphan P, Smollett K, Tong L, Orton R, Hughes J, Holland P, Silva V, Pascall DJ, Puxty K, da Silva Filipe A, Yebra G, Shaaban S, Holden MTG, Pinto RM, Gunson R, Templeton K, Murcia PR, Patel AH, Klenerman P, Dunachie S, Dunachie S, Klenerman P, Barnes E, Brown A, Adele S, Kronsteiner B, Murray SM, Abraham P, Deeks A, Ansari MA, de Silva T, Turtle L, Moore S, Austin J, PITCH Consortium, et al. 2022. SARS-CoV-2 Omicron is an immune escape variant with an altered cell entry pathway. *Nat Microbiol* 7:1161–1179. <https://doi.org/10.1038/s41564-022-01143-7>.
55. Gu Y, Cao J, Zhang X, Gao H, Wang Y, Wang J, He J, Jiang X, Zhang J, Shen G, Yang J, Zheng X, Hu G, Zhu Y, Du S, Zhu Y, Zhang R, Xu J, Lan F, Qu D, Xu G, Zhao Y, Gao D, Xie Y, Luo M, Lu Z. 2022. Receptome profiling identifies KREMEN1 and ASGR1 as alternative functional receptors

- of SARS-CoV-2. *Cell Res* 32:24–37. <https://doi.org/10.1038/s41422-021-00595-6>.
56. Jocher G, Grass V, Tschirner SK, Riepler L, Breimann S, Kaya T, Oelsner M, Hamad MS, Hofmann LI, Blobel CP, Schmidt-Weber CB, Gokce O, Jakwerth CA, Trimpert J, Kimpel J, Pichlmair A, Lichtenthaler SF. 2022. ADAM10 and ADAM17 promote SARS-CoV-2 cell entry and spike protein-mediated lung cell fusion. *EMBO Rep* 23:e54305. <https://doi.org/10.15252/embr.202154305>.
  57. Yamamoto M, Gohda J, Kobayashi A, Tomita K, Hirayama Y, Koshikawa N, Seiki M, Semba K, Akiyama T, Kawaguchi Y, Inoue JI. 2022. Metalloprotease-dependent and TMPRSS2-independent cell surface entry pathway of SARS-CoV-2 requires the furin cleavage site and the S2 domain of spike protein. *mBio* 13:e00519-22. <https://doi.org/10.1128/mbio.00519-22>.
  58. Kastenhuber ER, Mercadante M, Nilsson-Payant B, Johnson JL, Jaimés JA, Muecksch F, Weisblum Y, Bram Y, Chandar V, Whittaker GR, tenOever BR, Schwartz RE, Cantley L. 2022. Coagulation factors directly cleave SARS-CoV-2 spike and enhance viral entry. *Elife* 11:e77444. <https://doi.org/10.7554/eLife.77444>.
  59. Essalmani R, Jain J, Susan-Resiga D, Andréo U, Evagelidis A, Derbali RM, Huynh DN, Dallaire F, Laporte M, Delpal A, Sutto-Ortiz P, Coutard B, Mapa C, Wilcoxon K, Decroly E, Nq Pham T, Cohen ÉA, Seidah NG. 2022. Distinctive roles of furin and TMPRSS2 in SARS-CoV-2 infectivity. *J Virol* 96:e00128-22. <https://doi.org/10.1128/jvi.00128-22>.
  60. Gobeil SM, Janowska K, McDowell S, Mansouri K, Parks R, Stalls V, Kopp MF, Manne K, Li D, Wiehe K, Saunders KO, Edwards RJ, Korber B, Haynes BF, Henderson R, Acharya P. 2021. Effect of natural mutations of SARS-CoV-2 on spike structure, conformation, and antigenicity. *Science* 373:eabi6226. <https://doi.org/10.1126/science.abi6226>.
  61. Meng B, Kemp SA, Papa G, Dahir R, Ferreira I, Marelli S, Harvey WT, Lytras S, Mohamed A, Gallo G, Thakur N, Collier DA, Mlcochova P, Consortium C-GU, Duncan LM, Carabelli AM, Kenyon JC, Lever AM, De Marco A, Saliba C, Culap K, Cameron E, Matheson NJ, Piccoli L, Corti D, James LC, Robertson DL, Bailey D, Gupta RK, COVID-19 Genomics UK (COG-UK) Consortium. 2021. Recurrent emergence of SARS-CoV-2 spike deletion H69/V70 and its role in the Alpha variant B.1.1.7. *Cell Rep* 35:109292. <https://doi.org/10.1016/j.celrep.2021.109292>.
  62. Bussani R, Schneider E, Zentilin L, Collesi C, Ali H, Braga L, Volpe MC, Colliva A, Zanonati F, Berlot G, Silvestri F, Zaccogna S, Giacca M. 2020. Persistence of viral RNA, pneumocyte syncytia and thrombosis are hallmarks of advanced COVID-19 pathology. *EBioMedicine* 61:103104. <https://doi.org/10.1016/j.ebiom.2020.103104>.
  63. Davies NG, Jarvis CI, Group CC-W, Edmunds WJ, Jewell NP, Diaz-Ordaz K, Keogh RH, CMMID COVID-19 Working Group. 2021. Increased mortality in community-tested cases of SARS-CoV-2 lineage B.1.1.7. *Nature* 593:270–274. <https://doi.org/10.1038/s41586-021-03426-1>.
  64. Blanquart F, Hoze N, Cowling BJ, Debarre F, Cauchemez S. 2022. Selection for infectivity profiles in slow and fast epidemics, and the rise of SARS-CoV-2 variants. *Elife* 11:e75791. <https://doi.org/10.7554/eLife.75791>.
  65. McCallum M, Czudnochowski N, Rosen LE, Zepeda SK, Bowen JE, Walls AC, Hauser K, Joshi A, Stewart C, Dillen JR, Powell AE, Croll TI, Nix J, Virgin HW, Corti D, Snell G, Veesler D. 2022. Structural basis of SARS-CoV-2 Omicron immune evasion and receptor engagement. *Science* 375:864–868. <https://doi.org/10.1126/science.abn8652>.
  66. Zhang J, Cai Y, Lavine CL, Peng H, Zhu H, Anand K, Tong P, Gautam A, Mayer ML, Rits-Volloch S, Wang S, Sliz P, Wesemann DR, Yang W, Seaman MS, Lu J, Xiao T, Chen B. 2022. Structural and functional impact by SARS-CoV-2 Omicron spike mutations. *bioRxiv*. <https://doi.org/10.1101/2022.01.11.475922>.
  67. Bosen B, Legros V, Zhou B, Siret E, Mathieu C, Cosset FL, Lavillette D, Denolly S. 2021. The SARS-CoV-2 envelope and membrane proteins modulate maturation and retention of the spike protein, allowing assembly of virus-like particles. *J Biol Chem* 296:100111. <https://doi.org/10.1074/jbc.RA120.016175>.
  68. Rocheleau L, Laroche G, Fu K, Stewart CM, Mohamud AO, Côté M, Giguère PM, Langlois MA, Pelchat M. 2021. Identification of a high-frequency intra-host SARS-CoV-2 spike variant with enhanced cytopathic and fusogenic effects. *mBio* 12:e00788-21. <https://doi.org/10.1128/mBio.00788-21>.
  69. Crawford KHD, Eguia R, Dingens AS, Loes AN, Malone KD, Wolf CR, Chu HY, Tortorici MA, Veesler D, Murphy M, Pettie D, King NP, Balazs AB, Bloom JD. 2020. Protocol and reagents for pseudotyping lentiviral particles with SARS-CoV-2 spike protein for neutralization assays. *Viruses* 12:513. <https://doi.org/10.3390/v12050513>.